Chapter 9

SURFACE FLUXES FOR PRACTITIONERS OF GLOBAL OCEAN DATA ASSIMILATION

William B. Large
National Center for Atmospheric Research, Boulder, Colorado, USA

Abstract The ability of available ocean surface fluxes to meet the demands of the Global Ocean Data Assimilation Experiment (GODAE) for global, near real time, fields of known uncertainty is examined. Surface flux problems that are discussed in detail include the lack of direct surface measurements to serve as a standard, the difference between fluxes measured at height above the sea and the desired surface fluxes, the complications posed by the need for ocean-ice fluxes, and the large number of global fields required to describe the fluxes. The formulation of the air-sea, ocean-ice and air-ice fluxes of momentum, heat and freshwater, in terms of these fields is detailed from the measurements (including satellite based flux estimates) to the parameterizations. Air-ice fluxes are included to cover the possibility of coupling a sea-ice model within the data assimilation system. The position that there is no one set of flux products that represents the best possible choice for GODAE in all regions and all components is adopted. An alternative merger of a variety of different datasets is described along with objective corrections based on regional and/or short term observations, and ocean model behavior. A flux climatology based on these datasets and observed sea surface temperature is presented as the mean and variability from the seasonal to inter-annual, that GODA flux products should strive to reproduce. The necessary condition of near zero net global heat and freshwater climatological fluxes is demonstrated.

Keywords: Ocean flux measurement, parameterization, fields, climatology.

1. Introduction

Global Ocean Data Assimilation Experiment (GODAE) places rigorous demands on the surface flux forcing, not all of which can be entirely met. Most obvious, is the need for global coverage, including the poorly

sampled Southern Ocean and ice covered polar seas. Another challenge is proper specification of uncertainties. Also, the requirement for "near real time" fluxes precludes the use of some data, and makes this application very different from its cousin; Ocean Reanalysis. In both cases, flux variability should be properly represented across all the important ocean time scales; from the 12-hour polar inertial period, to the decadal, but GODAE may place a higher premium on time scales comparable to an assimilation cycle, such as the diurnal solar and three to seven day synoptic cycles.

Of primary importance are the surface fluxes of heat, Q, freshwater, F, and momentum, $\vec{\tau}$, with components τ_λ in the zonal and τ_ϕ in the meridional directions. Nearly all aspects of this rather complicated subject are comprehensively covered in the final report of the WCRP/SCOR Working Group on Air-Sea Fluxes (WGASF, 2000). With this report as a solid base, it is possible here to focus on what practitioners of GODAE should understand about the ocean surface fluxes they may utilize.

Perhaps the most well known constraint on surface fluxes is that the global long term heat and freshwater fluxes into the ocean should both be near zero. Observations of long-term changes in ocean heat content suggest a heat flux of at most a few W/m^2. For example, Levitus et al. (2000) find that the temperature of the world's oceans increased from the 1950s to the 1990s at a rate equivalent to a surface heat flux imbalance of only $0.3W/m^2$. Similarly, the global ocean salinity record doesn't support a significantly non-zero global long-term freshwater flux. However, fluxes on shorter time and space scales are not known nearly so well. This issue and other surface flux problems are outlined in Section 2. Sections 3 and 4 deal with the measurement and parameterization of the turbulent flux components. Satellite techniques have been most successful at estimating the radiative heating, precipitation and wind stress, so only these products are discussed in Section 5.

Section 6 is concerned with what the various surface flux fields might really look like. Any specified surface forcing will be incremented by the data assimilation cycle. The resulting fluxes should at least satisfy global constraints and should be compared to existing air-sea flux climatologies to see if there are unacceptably large discrepancies in seasonal cycles, variability on inter-annual and longer time scales, and the mean. A number of such climatologies are compared by Beranger et al. (1999); including the SOC (Southhampton Oceanography Centre; Josey et al. 1998), COADS (University of Wisconsin-Milwaukee version of the Cooperative Ocean Atmosphere Data Set; Da Silva et al., 1994), NCEP (NCEP/NCAR reanalysis fluxes; Kalnay et al., 1996) and ERA-15 (15 year ECMWF reanalysis fluxes, Gibson it al., 1997). Others can be

found in WGASF (2000) and fluxes from the recent 40 year ECMWF reanalysis (ERA-40) are beginning to appear. Different fields from various datasets have been corrected for known biases and merged (Large and Yeager, 2004) to produce the fluxes presented in Section 6. Although sea-ice concentration has been well observed from satellites since the late 1970s, other necessary ice data (e.g. thickness and surface temperature) are not available to compute companion air-ice and ice-ocean flux climatologies.

2. Ocean surface flux problems

The fundamental problem of ocean surface forcing is that it can not be directly observed. In the case of the momentum flux between the atmosphere and a uniform land surface, it is possible to construct a "drag plate" (Bradley, 1968) and actually observe the wind stress over a small area, at high frequency. This standard can then be transferred to less direct, more easily implemented measurement techniques such as eddy correlation (Haugen et al., 1971), which themselves can be used as a transfer standard to even more indirect and easily implemented methods, such as inertial dissipation (Large and Pond, 1981). The problem for GODAE is that there are no prospects for an ocean surface drag plate. It is conceivable that detailed measurements of heat and moisture changes over a small patch of ground could yield direct estimates of the heat and water fluxes that could serve as a basic truth standard. Unfortunately, a similar approach in the ocean appears hopeless, largely because of transports across the non-surface boundaries of the control volume, and also because of the vertical penetration of solar radiation and the presence of bubbles that are carried to depth after wave breaking. At the end of the transfer of standard chains are the bulk aerodynamic formulae (Roll, 1966), whose inputs are relatively easily measured mean quantities such as atmospheric wind speed, U, potential temperature, θ, and specific humidity, q, as well as sea surface temperature (SST). But, without a direct standard there always remains an unquantified uncertainty in estimates of ocean surface fluxes.

Since the nature of the sea surface dictates that flux measurements be made at some distance, d of order 10 m above the sea surface, there is another basic problem; namely, this flux is not equal to the surface flux. To estimate the fractional error in wind stress, $\delta\tau = |\tau - \tau(d)|/\tau$, consider the momentum equation for a mean near surface wind, U, aligned with the x-coordinate axis. The dominant terms in horizontally homogeneous flow are (Busch, 1977)

$$\rho \ \partial_t U \ = \ \partial_z \tau(z) \ - \ \partial_x P_o \ , \tag{1}$$

where ρ and P_o are atmospheric density and pressure, respectively, and $\tau(z)$ is the downstream stress as a function of height, z. Except near the equator, the geostrophic winds aloft, U_g, are found empirically to be about 30% greater than $U(d)$, and rotated by about 16° (Deacon, 1973):

$$\rho \ f \ U_g \ = \ \partial_n P_o \ = \ \partial_x P_o / \ sin(16^\circ) \ = \ \rho \ f \ 1.3 \ U(d) \ , \qquad (2)$$

where f $\approx 10^{-4} s^{-1}$, is the Coriolis parameter and n is a horizontal coordinate perpendicular the direction of U_g. In steady flow, $\partial_t U = 0$, substitution of (2) into (1) gives

$$\begin{aligned} \delta\tau \ &= \ 1.3 \ d \ f \ sin(16^\circ) \ \frac{\rho \ U(d)}{\tau} \\ &\approx \ 0.04 s^{-1} \ d/U(d) \ , \end{aligned} \qquad (3)$$

where measurements over the sea have been used to approximate $\rho \, U(d)/\tau$ with $1000/U(d)$. Thus, ship measurements of stress at say d = 15 meters should be systematically biased low by 15% at a wind speed of $U(d) = 4m/s$. This problem becomes more complicated in unsteady winds, with (1) showing the error due to flux divergence increasing during falling winds and decreasing on the rising wind. Despite the approximations, the above exercise does illustrate that there is no such region as a "constant flux layer". Indeed, Lumley and Panofsky (1964) introduce the term only to describe the region where measurement error is expected to be greater than the loss of flux with height. Similar consideration of the heat and moisture equations show that heat and moisture fluxes are not, in general, constant with height either.

A third problem is that truly global ocean data assimilation is greatly complicated by the presence of sea-ice at polar latitudes. Not only do ice-ocean fluxes become involved, but the freezing of sea-water and brine rejection need to be accounted for. An attractive, but complicated approach is to include a Sea-Ice Model (SIM) in the assimilation system, so that ice-ocean fluxes are explicitly computed and exchanged as part of the coupling. However, it then becomes necessary to force the SIM with air-ice fluxes of heat, freshwater and momentum. This option places very high demands on flux accuracies, because of positive feedbacks associated with sea-ice. A simpler procedure is just to specify reasonable ice-ocean fluxes even though they are neither routinely observed, nor well known.

The final Ocean Surface Flux problem to be considered is the proliferation of fields that are required to capture the physics and to take full advantage of the available observations. Clearly, the simplest GODAE scheme would follow the Stammer et al. (2002) Ocean Reanalysis example and utilize global fields of the four fluxes; Q, F, τ_λ and τ_ϕ from

Numerical Weather Prediction (NWP), but important physics is lost. In general, a fraction, f_i, of the ocean surface may be covered by sea-ice, leaving a fraction, $f_o = 1 - f_i$, exposed to the atmosphere above. The ocean surface fluxes are, therefore, given by

$$\begin{aligned} Q &= f_i\, Q_{io} + f_o\, Q_{as} \\ F &= f_i\, F_{io} + f_o\, F_{as} + R \\ \vec{\tau} &= f_i\, \vec{\tau}_{io} + f_o\, \vec{\tau}_{as}\ , \end{aligned} \tag{4}$$

where the subscripts "as" and "io" denote air-sea and ice-ocean fluxes, respectively. In (4), R is the continental runoff. The number of required fields has already expanded from 4 to 10, and there are further increases as the air-sea, ice-ocean and air-ice fluxes are explored individually below.

2.1 Air-sea fluxes

The air-sea heat flux has radiative (shortwave and longwave), turbulent (sensible and latent) and particle components, which are all defined here as positive when they act to heat the ocean. Similarly, water fluxes (precipitation, evaporation and runoff) are positive when they add water to the ocean. The wind stress is a turbulent flux aligned to the vector difference between $\vec{U}(d)$ and the ocean surface current, $\vec{U}_0$. A major complication for GODAE is that air-sea heat and freshwater fluxes need to be broken down into estimates of their components, namely;

$$\begin{aligned} Q_{as} &= Q_S + Q_L + Q_E + Q_H + Q_P \\ F_{as} &= P + E, \end{aligned} \tag{5}$$

because the penetration of solar radiation, Q_S into the upper ocean is an important process governing the evolution of SST (Denman and Miyake, 1973) and evaporation, E, from the ocean surface is accompanied by a latent heat flux, $Q_E = -\Lambda E$, where $\Lambda = 2.5 \times 10^6 j/kg$ is the latent heat of vaporization. Delivery of near real time estimates of all these components to a GODAE system is a daunting challenge. Instead, at least some degraded products will need to be used, but then the difficulty will be to specify the appropriate uncertainty. The growth of air-sea flux fields from 4 to as many as 14 is shown in Table 1.

Solar radiation includes wavelengths between 0.3 and 3μ and is always positive. It passes through the atmosphere where it is attenuated, mainly by clouds, before reaching the surface as solar insolation, Q_I, and the surface albedo (α) is the fraction that is reflected back to the atmosphere. About 40% of this insolation is diffuse, with an albedo $\alpha_{df} = 0.06$ (Payne,

Fluxes	Air-sea	Components	Fields	Bulk	
Q					Net Surface Heat Flux
	Q_{as}				Air-Sea Heat Flux
		Q_S			Net Solar Radiation
			Q_I		Solar Insolation
			α		Solar Albedo
		Q_L			Net Longwave Radiation
			Q_A		Downwelling Longwave
			SST_s		Skin SST
		Q_E^*			Latent Heat Flux
		Q_H^*			Sensible Heat FLux
F					Net Surface Freshwater Flux
	F_{as}				Air-Sea Freshwater Flux
		P			Total Precipitation
			P_R		Rainfall
			P_S		Snowfall
		E^*			Evaporation
		R	R		Continental Runoff
$\vec{\tau}$					Surface Wind Stress
	$\vec{\tau_{as}}^*$				Air-Sea Wind Stress
				$\vec{U}$	Wind Vector
				θ	Potential Air Temperature
				q	Air Specific Humidity
				P_o	Atmospheric Pressure
				SST_b	Bulk SST
				$S\vec{S}U$	Sea Surface Current

Table 1. Proliferation of air-sea flux fields from the four in the AIR-SEA column. Component fluxes denoted with an asterisk are parameterized by Bulk Aerodynamic Formulae in terms of the 7 parameters, including 2 wind components, in the BULK column. Other flux components are given by the 7 specified fields in the FIELD column.

1972). The albedo for the remaining direct solar radiation, α_{dr} varies with the solar zenith angle. The solar energy transferred to the ocean is then given by

$$Q_S \;=\; Q_I \;[\; 0.6\;(1-\alpha_{dr}) \;+\; 0.4\;(1-\alpha_{df})] \;\;=\;\alpha\;Q_I. \qquad (6)$$

At the temperature of the ocean surface and of the atmosphere above, blackbody radiation occurs at longer wavelengths (up to 50μ) and comprises the net longwave radiation,

$$Q_L \;=\; Q_A \;-\; \epsilon\;\sigma\;\;(SST)^4\;\;. \qquad (7)$$

In (7), the downwelling (positive) radiation from the atmosphere, Q_A, increases with cloud cover. The upwelling radiation from the ocean is given by $(-\epsilon\sigma(SST)^4\;)$, where $\sigma = 5.67\times10^{-8}W/m^2/K^4$ is the Stefan-Boltzmann constant and taking the surface emissivity ϵ as 1, accounts for reflected Q_A (Lind and Katsaros 1986). This high emissivity and the usually warmer SST compared to the radiating atmosphere and clouds, makes Q_L negative.

Since SST is a product of GODAE, the radiative flux problem can be thus reduced to one of specifying Q_I, α and Q_A (Table 1). Fortunately, these fields have been derived from satellite observations over the ocean (Section 5), so that there is no need to use empirical formulae, such as those developed by Smith and Dobson (1984) and examined by Fung et al. (1984). Nonetheless, these expressions do quantify to first order the decrease in Q_I and the increase in Q_A due to clouds. The compensating effect on the daily surface heat flux can be nearly complete in some situations. Therefore, it is important to use consistent data sets for both radiation components, so that errors due to clouds are minimized.

The sea surface is usually warmer than the overlying air, leading to an upward (negative) molecular diffusion of heat across the surface. At the same time evaporation from the surface is assumed to keep the surface air saturated, and hence usually more moist that the air above. These gradients are maintained by the vertical turbulent transports of sensible heat flux and moisture (latent heat), which in steady state must match the surface sensible heat flux, Q_H, and E (Q_E), respectively. Except in the rare circumstance of very warm moist air over a cold sea, evaporation takes water from the ocean and cools.

The major particle fluxes are precipitation, P, over the ocean due to rain, P_R and snow, P_S:

$$P \;=\; P_R \;+\; P_S. \qquad (8)$$

These fluxes are positive definite and account for about 90% of the evaporation (WGASF, 2000). Snowfall has an associated negative particle

heat flux, because the ocean must lose heat to melt it according to

$$Q_P \;=\; -\Lambda_f \; P_S, \tag{9}$$

where $\Lambda_f = 3.337 \times 10^5 j/kg$ is the latent heat of fusion. This flux can also include the temperature difference between the precipitation and SST. The in situ measurement of marine precipitation is very difficult (Knox, 1991), and further complicated by very serious sampling issues arising from its intermittency in both time and space. Also, problematic is the partitioning into rain and snow, because some data sets just give the total.

2.2 Ice-ocean fluxes

A comprehensive review of ice-ocean coupling is provided by Schmidt et al. (2004). Over much of the ice pack, especially in the Southern Ocean, the force balance of sea-ice is primarily between wind stress and ocean drag, which is referred to as free drift. For GODAE purposes it may be sufficient to assume that the air-ice stress, $\vec{\tau}_{ai}$ passes unchanged to the ocean:

$$\vec{\tau}_{io} \;=\; \vec{\tau}_{ai} \tag{10}$$

Otherwise internal ice rheology becomes involved in very computationally expensive calculations of internal ice stresses that are often small.

In general the ocean gains heat and salt where ice is formed and is cooled and diluted where the ice melts. The heat and salt fluxes are given by :

$$\begin{aligned} Q_{io} \;&=\; Q_M \;+\; Q_F \;+\; Q_B \;+\; Q_{PS} \\ F_{io} \;&=\; F_M \;+\; F_F \;+\; F_B. \end{aligned} \tag{11}$$

The fluxes associated with the melting of both sea-ice and accumulated snow are a cooling melt flux $Q_M < 0$ and positive freshwater flux $F_M > 0$. Solar radiation is able to penetrate thin ice to become an ocean surface flux, Q_{PS}. The usually cold atmosphere above the ice produces basal ice and a freshwater flux, $F_B < 0$, from the ocean. The corresponding ocean surface heat flux, Q_B, is usually near zero, because the basal cooling is balanced by the latent heat of fusion of the basal ice. Direct air-sea cooling of the ocean allows the possibility for ocean temperatures to fall below freezing. The physical process that relieves this unphysical condition is the formation of frazil sea-ice. A heat flux $Q_F > 0$ effectively restores the ocean temperature to the freezing point. Most of the salt is left behind and is represented by a negative freshwater flux, $F_F < 0$. Frazil ice formation can be a dominant process along the

coast of Antarctica where offshore winds can keep significant portions of the ocean surface ice-free.

2.3 Air-ice fluxes

Including a SIM within the GODAE system eliminates the need to specify ice-ocean fluxes, though observed sea-ice fraction should probably be assimilated, but requires data sets for computing all the air-ice fluxes. In general a sea-ice model has a number of ice categories. The air-ice heat and water fluxes for a particular ice category, n, are given by

$$\begin{aligned} Q^n_{ai} &= Q^n_S + Q^n_L + Q^n_E + Q^n_H \\ F^n_{ai} &= P^n + E^n \end{aligned} \tag{12}$$

Ice models differentiate between snow and rain. The former becomes P^n in (12), which accumulates in the snow layer atop ice category, n, with surface temperature, T^n_S, while the rain is often passed directly to the ocean below, as a contribution to F_{io} in (4).

Given a shortwave insolation data set, ice models typically split this radiation into four components; visible (wavelengths from 0.3 to 0.7μ) direct, visible diffuse, near-infrared (0.7 to 3μ) direct and near-infrared diffuse. An ice model then must provide the respective albedos; α^n_{Vdr}, α^n_{Vdf}, α^n_{Ndr} and α^n_{Ndf}, for each ice category, n. In order to use Q_I data the respective fractions are needed, with $.29, .24, .31, .16$ an acceptable partitioning:

$$Q^n_S = Q_I\,[.29(1-\alpha^n_{Vdr})+.31(1-\alpha^n_{Vdf})+.24(1-\alpha^n_{Ndr})+.16(1-\alpha^n_{Ndf})]. \tag{13}$$

It is simpler to utilize downwelling long-wave radiation, because there is no need to do any partitioning. The net long-wave radiation becomes:

$$Q^n_L = \epsilon_i\, Q_A - \epsilon_i \sigma (T^n_S)^4, \tag{14}$$

where $\epsilon_i = 0.95$, is the ice/snow emissivity. This emissivity is also used in the first term on the right-hand-side of (14) as 1 minus a longwave albedo.

2.4 Continental runoff

Very complex estuarine process govern runoff into the ocean, and may be beyond the scope of GODAE. However, it is important to capture the concentration near coastlines, especially at the mouths of large rivers. There should also be a representation of seasonality, including the storage of snowfall. For example, extratropical runoff can be made to peak

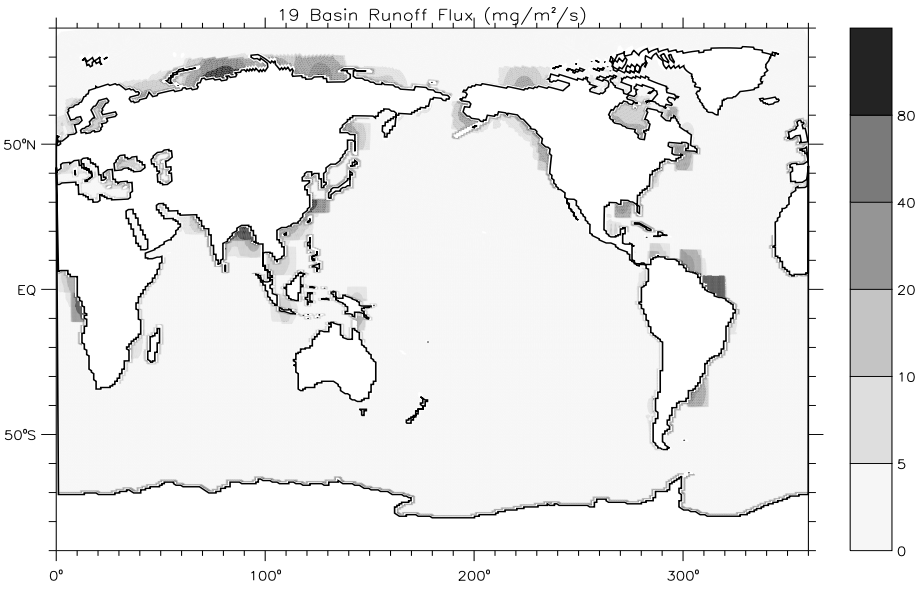

Figure 1. Distribution of the freshwater flux due to climatological runoff from continents. The flux unit of $1mg/m^2/s$ ($0.0864mm/day \approx 31mm/year$) is used, because it makes about the same contribution to the density flux as 1 W/m^2 of heat flux. Note the non-linear scale.

in late spring, and the Amazon in February (UNESCO, 1985). There are runoff data for approximately the largest 1000 of the world's rivers (e.g. Perry et al. 1996), which accounts for as much as 95% of the runoff from both South America and Europe into the Atlantic Ocean, but less than 5% from Australia and Antarctica. The remainder enters the ocean as ground water seepage, or as ungauged surface runoff, including icebergs. Therefore, it is necessary to have estimates of the net excess of precipitation over evaporation from each continent (e.g. Baumgartner and Reichel, 1975) and to distribute this excess as runoff into the bordering ocean basins using river routing schemes and flow estimates (e.g. Fekete, et al., 1999).

A practical treatment of runoff from 19 drainage basins (Large and Yeager, 2004), as an ocean surface flux is shown in Fig. 1. The ungauged runoff is distributed evenly along the coast of each basin. The gauged river runoff is spread over ocean grid-cells near the measurement site, so as to give an ocean surface salinity signature that is similar to that seen observations such as the Levitus et al. (1998) World Ocean Atlas 98 (WOA98). This procedure mimics the flow of fresh estuarine

water over the salty coastal sea-water and avoids excessively low salinities at OGCM grid-points at river mouths. Rivers such as the Amazon, Ganges/Brahmaputra, Zaire, Yenisei/Ob and Yangtze, contribute to the surface density flux in an major way. They each give local freshwater fluxes in excess of $100 mg/m^2/s$ ($1 mg/m^2/s \approx 31 mm/year$), which produces a density flux approximately equivalent to that of a $100 W/m^2$ heat flux. Averaged over the entire ocean area of $3.523 \times 10^8 km^2$ the equivalent freshwater flux is $3.57 mg/m^2/s$, or about 11 cm/year.

3. Measuring turbulent air-sea fluxes

The portion of a geophysical fluid that is directly influenced by the presence of a boundary is referred to as a planetary boundary layer (PBL) and the two most notable examples are the atmospheric (ABL) and oceanic (OBL). Air-sea turbulent fluxes are actually measured in the atmospheric surface layer which begins above the direct influence of the surface roughness elements and ends at about 10% of the ABL height. The semi-empirical Monin-Obukhov similarity theory is the basis of our understanding of the physics of this turbulent layer. The theory argues that in the surface layer the only important turbulence parameters are the height, z, and the air-sea fluxes. The fundamental turbulent parameters that can be formed from the fluxes are the friction velocity, u^*, the scales of the turbulent fluctuations of scalars, such as potential temperature, θ^*, and specific humidity, q^*, and the Monin-Obukhov length scale, L:

$$\begin{aligned} u^{*2} &= |\vec{\tau}|/\rho \\ u^*\theta^* &= Q_H/(\rho\ c_p) \\ u^*q^* &= Q_L/(\rho\ \Lambda) \\ L &= u^{*3}/(\kappa\ B_o), \end{aligned} \tag{15}$$

where $\kappa = 0.4$ is von Karman's constant and c_p is the specific heat of the air. The surface buoyancy flux is given by the latent and sensible heat fluxes and can be expressed as

$$B_o = g\ u^*\ [\frac{\theta^*}{\theta_v} + \frac{q^*}{(q + 0.608^{-1})}\ ]\ , \tag{16}$$

where g is gravitational acceleration, $\theta_v = \theta\ (1. + .608q)$ is the virtual potential temperature and the factor 0.608 is the ratio of the molecular weights of dry air and of water vapor minus 1.

Dimensional analysis is very powerful in the surface layer because the number of parameters is small and comparable to the number of physical dimensions. It predicts that layer structure when appropriately scaled

(non-dimensionalized) by z, u^*, θ^*, q^* and L should be functions of the non-dimensional group $\zeta = z/L$. With all the scales common to all surface layer flows, the structure of any layer and its turbulence, according to the theory, must always be "similar", with any dependencies on ζ universal. The most important consequences are the familiar logarithmic vertical profiles of mean wind (Tennekes, 1973), temperature and humidity. Scaling the mean property gradients gives :

$$\frac{\kappa\ z}{u^*}\ \partial_z U\ = \phi_m(\zeta)\ ;\ \ \frac{\kappa\ z}{\theta^*}\ \partial_z \theta\ = \phi_s(\zeta)\ ;\ \ \frac{\kappa\ z}{q^*}\ \partial_z q\ = \phi_s(\zeta)\ , \qquad (17)$$

where κ sets the non dimensional profiles for momentum, $\phi_m(\zeta)$, and for scalars, $\phi_s(\zeta)$ equal to 1 at neutral stability, $\zeta = 0$. These functions of the stability parameter, ζ, have been determined empirically, and acceptable fits to the data for present purposes are (Högström, 1988) :

$$\begin{aligned} \phi_m\ =\ \ \ \ \phi_s\ \ &=\ 1\ +5\ \zeta && \zeta > 0 \\ \phi_s\ =\ \phi_m^2\ \ \ \ &=\ (1-16\zeta)^{-\frac{1}{2}} && -1 < \zeta < 0\ . \end{aligned} \qquad (18)$$

The uncertainty in these functions are a major problem with inferring fluxes (u^*, θ^* and q^*) from measurements of mean property gradients. Other serious issues with "the profile method" are the need for very accurate instrumentation, the small signals (gradients) except near the surface, and the danger of measuring below the surface layer.

Integration of these gradient relations (Paulson, 1970) gives the mean property profiles in the surface layer, but not below,

$$\begin{aligned} U(z)\ \ &=\ SSU + \tfrac{u^*}{\kappa}\ \ [ln(z/z_o) - \psi_m(\zeta)] \\ \theta(z)\ \ &=\ SST + \tfrac{\theta^*}{\kappa}\ \ [ln(z/z_\theta) - \psi_s(\zeta)] \\ q(z)\ \ &=\ SSQ + \tfrac{q^*}{\kappa}\ \ [ln(z/z_q) - \psi_s(\zeta)]. \end{aligned} \qquad (19)$$

The constants of integration, z_o, z_θ and z_q, are the roughness lengths, that fully describe the surface as seen by the flow in the surface layer. The integrated non-dimensional profiles for $Y\ =\ (1\ -\ 16\ \zeta)^{1/4}$ are:

$$\begin{aligned} \psi_m\ \ \ \ \ \ \ \ &=\ \psi_s\ =\ -\ 5\ \zeta && \zeta > 0 \\ \psi_m(\zeta)\ \ &= 2ln(\tfrac{1+Y}{2}) + ln(\tfrac{1+Y^2}{2}) - 2\ tan^{-1}(Y) + \tfrac{\pi}{2} && -1 < \zeta < 0 \\ \psi_s(\zeta)\ \ \ \ \ \ &=\ 2\ ln(\tfrac{1+Y^2}{2}) && -1 < \zeta < 0. \end{aligned} \qquad (20)$$

3.1 Eddy covariance

Vertical transport through a PBL is accomplished by three dimensional turbulent eddies. At a fixed point their frequency is related to the

downstream radian wavenumber, k, by Taylor's frozen turbulence hypothesis, $k = 2\pi f/U$. The time average of a vertical flux of property X at a point is the integral over frequency, f, of the cospectrum, $\Phi_{wx}(f)$, of the property fluctuations, x, and the vertical velocity, w. Similarly, the spatial average at a point in time is the integral of the cospectrum over k. In practice, the eddies occupy a finite range of wavenumber space, say k_1 to k_2, and hence frequency space, say f_1 to f_2, so the fluxes become

$$u^*\ x^* = \int_{f_1}^{f_2} \Phi_{wx}(f)df\ = \int_{k_1}^{k_2} \Phi_{wx}(k)dk\ = \int_{f_1}^{f_2}\int_{k_1}^{k_2} \Phi_{wx}(f,k)dk\ df. \tag{21}$$

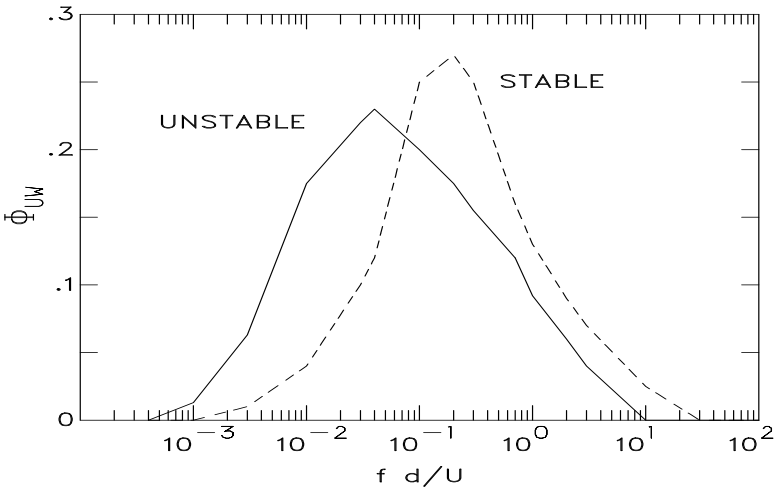

Figure 2. Observed momentum flux cospectra at 13m height in the ABL ensemble averaged over 88 stable and 108 unstable realizations. The ordinate is normalized and is variance preserved by multiplying by f/u^{*2}. The non-dimensional abscissa is natural frequency, fd/U.

Eddy covariance measurements of the sensible heat flux ($X = \rho\, c_p\, \theta$), latent heat ($X = \rho\ \Lambda\ q$) and momentum ($X = \rho\ U$) are not as straightforward as they might appear. In addition to having to work at a height, d, it is often necessary to compromise between sampling long enough to compute a statistically representative flux while not sampling through a change in flow regime. To illustrate, an ensemble average of cospectra, Φ_{uw}, observed at about 13m height over the ocean are shown in Fig. 2 for both stable ($\zeta > 0$) and unstable ($\zeta < 0$) conditions. As the boundary is approached the flux transporting eddies become confined to "fit" within the height, d, and so become smaller in wavelength (higher wavenumber and frequency). This effect is removed in the ensemble by scaling the frequency by a factor, d/U. The Fig. 2 ensembles

indicate that the limits of integration should be about $f_1 = 4 \times 10^{-4} U/d$ and $f_2 = 30U/d$. An ensemble of heat flux cospectra is similar, with the same stability dependence (*e.g.,* Large and Pond, 1982). Thus at a given height the same five decades of eddy sizes transport both the heat and the momentum vertically. However, these limits may not apply to an individual realization, where the low frequency cospectrum can be large and of opposite sign than the integral. There is no standard treatment of such cases, which adds an element of uncertainty that is difficult to quantify without the benefit of a direct flux measurement. Practical problems with eddy covariance measurements include the accuracy, response (set by f_2) and orientation of the sensors, especially on ships and buoys at sea. It is critical to know the alignment with the vertical so that the measured vertical velocity is not seriously contaminated by the much larger horizontal velocity. This problem is particularly acute in the case of the momentum flux, because erroneous U in the w measurement correlates perfectly with u. The distortion of boundary layer flow by large platforms such as ships raises similar issues as orientation.

3.2 Inertial dissipation

The inertial dissipation method is particularly well suited to moving platforms at sea, because the vertical velocity is not involved, and a considerable degree of flow distortion can be tolerated. It is relatively indirect, but can be regarded as an acceptable standard because of extensive comparison with eddy correlation measurements from stable platforms where flow distortion was minimal (e.g. Large and Pond, 1981; Yelland and Taylor, 1996). Measurements of the various terms in the turbulent kinetic energy equation find that to a very good approximation the dissipation, ϵ, equals the mechanical production minus the buoyant suppression, B_o :

$$\epsilon = u^{*2}\, \partial_z U - B_o = \tfrac{u^{*3}}{\kappa\, z}\, \phi(\zeta) - \tfrac{u^{*3}}{\kappa\, L} \tag{22}$$

$$u^{*3} = \kappa\, z\, \epsilon\, (\phi_m(\zeta) - \zeta)^{-1}\ , \tag{23}$$

where (15) and (17) have been used for substitution. Similarly, dissipation equals production of scalar variance for X=$[\theta, q]$ gives

$$N_x = u^*\, x^*\, \partial_z X = \frac{u^*\, x^{*2}}{\kappa\, z}\, \phi_s(\zeta) \tag{24}$$

$$x^{*2} = \kappa\, z\, N_x\, [u^*\, \phi_s(\zeta)]^{-1}\ . \tag{25}$$

Thus, the surface flux measurement is transformed into measuring ϵ, and the dissipation rates of scalar fluctuations, N_θ and N_q. Direct dissipation measurements are difficult, because they involve centimeter scales.

Fortunately, they can be inferred from spectra of fluctuations at frequencies in the Kolmogoroff (-5/3) range. Invoking Taylor's hypothesis the frequency spectra in this range become:

$$\begin{aligned} \Phi_u(f) &= K' \, \epsilon^{\frac{2}{3}} \, (\tfrac{2\pi}{U})^{-\frac{2}{3}} \;\; f^{-\frac{5}{3}} \\ \Phi_x(f) &= \beta_x \, N_x \, \epsilon^{-\frac{1}{3}} \, (\tfrac{2\pi}{U})^{-\frac{2}{3}} \;\; f^{-\frac{5}{3}} \; . \end{aligned} \tag{26}$$

The empirical Kolmogoroff constants are $K' = 0.55$, and $\beta_\theta = \beta_q = 0.80$.

The Kolmogoroff range begins at about $fd/U = 0.2$, so the sensors must have a relatively fast sampling capability, of order 10Hz. Multiple measurements across frequency allows the existence of the $-5/3$ range to be checked, and contaminated data, by flow interference for example, to be discarded. The method can be regarded as a physically based parameterization of the fluxes in terms of high frequency turbulent fluctuations, with eddy correlation comparisons essential for verifying the assumptions and empirical constants, and for transferring the measurement standard.

4. Bulk aerodynamic formulae

How well can the turbulent surface fluxes be estimated from time and/or space average (bulk) measures (Table 1) from the turbulent surface layer? Since such data are likely to be a major input of GODAE systems, this question needs to be addressed in detail. Bulk transfer coefficients for momentum, sensible heat and moisture transfer, are defined, respectively, as

$$C_D \; = \; \frac{u^{*2}}{(\Delta U)^2} \quad ; \quad C_H \; = \; \frac{u^* \; \theta^*}{\Delta U \;\; \Delta\theta} \quad ; \quad C_E \; = \; \frac{u^* \; q^*}{\Delta U \;\; \Delta q} \; , \tag{27}$$

where $\Delta U = |\vec{U}(z) - \vec{U_o}|$, $\Delta\theta = \theta(z) - SST$ and $\Delta q = q(z) - SSQ$ are the air - sea differences. Substitution of the profile equations (19) gives

$$C_D \; = \frac{\kappa^2}{[ln(\frac{z}{z_o}) - \psi_m]^2} \; ; \;\; C_H \; = \frac{\kappa\sqrt{C_D}}{[ln(\frac{z}{z_\theta}) - \psi_s]} \; ; \; C_E \; = \frac{\kappa\sqrt{C_D}}{[ln(\frac{z}{z_q}) - \psi_s]} \; , \tag{28}$$

which demonstrates the dependencies on height, stability and the roughness lengths. In an ideal world of plentiful, reliable measurements the coefficient estimates would be binned according to height and stability and the roughness dependencies determined for each bin. Unfortunately, even the above indirect flux estimates are too difficult, expensive and rare. Therefore, most coefficient determinations are shifted to 10m

height and neutral stability, where the three coefficients become;

$$C_{DN} \;=\; \frac{\kappa^2}{[ln(\frac{10m}{z_o})]^2} \;\; ; \; C_{HN} \;=\; \frac{\kappa\sqrt{C_{DN}}}{ln(\frac{10m}{z_\theta})} \;\; ; \; C_{EN} \;=\; \frac{\kappa\sqrt{C_{DN}}}{ln(\frac{10m}{z_q})} \;\; . \quad (29)$$

The transfer coefficients and their 10m, neutral equivalents can be related by eliminating z_o, z_θ and z_q from (28) and (29) :

$$\begin{aligned} C_{DN} \;&=\; C_D \; (1 + \tfrac{\sqrt{C_D}}{\kappa} \; [ln(\tfrac{10m}{z}) + \psi_m(\zeta)])^{-2} \\ C_{HN} \;&=\; C_H \; \sqrt{\tfrac{C_{DN}}{C_D}}(1 + \tfrac{C_H}{\kappa\sqrt{C_D}} \; [ln(\tfrac{10m}{z}) + \psi_s(\zeta)])^{-1} \\ C_{EN} \;&=\; C_E \; \sqrt{\tfrac{C_{DN}}{C_D}}(1 + \tfrac{C_E}{\kappa\sqrt{C_D}} \; [ln(\tfrac{10m}{z}) + \psi_s(\zeta)])^{-1} \; . \end{aligned} \quad (30)$$

The roughness length dependencies of these coefficients have been explored using many data sets, but rarely with combined data. This search has not been conducted in a single standard way, so often the procedure, rather than the data, is responsible for differences in results. The better approaches begin by defining the equivalent 10m, neutral wind, U_N, temperature, θ_N, and humidity, q_N, relative to the sea surface, in terms of the turbulent flux scales and 10m, neutral transfer coefficients :

$$U_N^2 \;=\; \frac{u^{*2}}{C_{DN}} \; ; \; \theta_N \;=\; \frac{u^* \; \theta^*}{C_{HN} \; U_N} \; ; \; q_N \;=\; \frac{u^* \; q^*}{C_{EN} \; U_N} \quad (31)$$

$$U_N^2 \;=\; \frac{C_D}{C_{DN}}(\Delta U)^2 \; ; \; \theta_N \;=\; \frac{C_H}{C_{HN}} \; \frac{\Delta U}{U_N} \; \Delta\theta \; ; \; q_N \;=\; \frac{C_E}{C_{EN}} \; \frac{\Delta U}{U_N} \; \Delta q \;\; . \quad (32)$$

There is no consensus on how to proceed from this point. To illustrate, consider the following drag coefficient formulation. Perform a multiple regression analysis of u^{*2} on U_N, U_N^2, U_N^3, ... , to find coefficients of the polynomial

$$u^{*2} \;=\; a_0 \;+\; a_1 \; U_N \;+\; a_2 \; U_N^2 \;+\; a_3 \; U_N^3 + ... \quad (33)$$

After combining data from multiple sources to span a range of wind speeds from less than $1m/s$ to more than $25m/s$, Vera (unpublished manuscript, 1986) found that coefficients of the fourth power and higher were not statistically significant. Consistent with the principle of no net stress over space and/or time of zero wind speed neither was a_0, leaving $a_1 = 0.00270m/s$, $a_2 = 0.000142$ and $a_3 = 0.0000764s/m$ as the only nonzero coefficients. Division by U_N^2 yields

$$C_{DN} \;=\; a_1/U_N \;+\; a_2 \;+\; a_3 \; U_N \; , \quad (34)$$

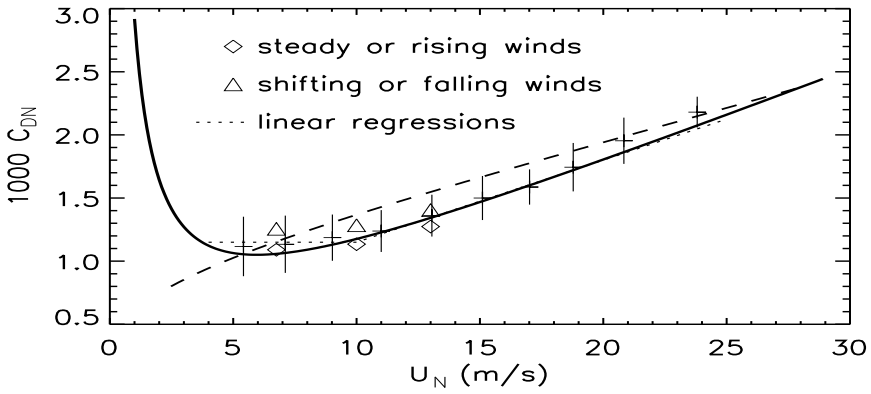

Figure 3. Neutral 10m drag coefficient as a function of equivalent neutral 10m wind speed; as observed (pluses extending ±1 standard deviation about the mean over wind speed bands), the observed means during steady or rising winds (diamonds) and for shifting and falling winds (triangles), and as formulated from piecewise linear regression of all these data (dotted lines), from Eq. (34) (solid curve) and from Eq. (36) (dashed curve).

which is plotted in Fig. 3 (thick solid curve) in a form that can be compared to the alternatives shown and discussed by WGASF (2000).

At low winds the surface stress is supported by molecular viscous stress, independent of the roughness elements. In such aerodynamically smooth flow, the emergence of kinematic viscosity, ν, as a parameter leads to the non-dimensional group :

$$z_o \; u* / \nu \;=\; \alpha_s \quad , \tag{35}$$

where $\alpha_s \approx 0.11$ is an empirical constant. From (29) C_{DN} becomes inversely proportional $(z_o \, U_N)^2$, and grows without bound, as this factor approaches zero at very low wind speeds, consistent with (34) and Fig. 3.

A more common practice has been to linearly regress C_{DN} on U_N, but data from higher winds (e.g. $U_N > 12m/s$) give a steeper slope than lower winds. Therefore, linear regressions are meaningful only over narrow wind speed ranges, and could be used to form a piecewise linear formulation (Fig. 3, dotted; Trenberth et al., 1989). Another approach is to fit data to proposed functional forms of the roughness length. An early form (Charnock, 1955) assumes that all important features of the ocean surface wave field are captured by gravitational acceleration, which leads to the non-dimensional group :

$$z_o \; g \; u^{*-2} \;=\; \alpha_c \quad , \tag{36}$$

where α_c is constant. Garratt (1977) fits a variety of data and suggests $\alpha_c = 0.0144$ (Fig. 3 dashed curve), but Stewart (1974) notes that for

winds below $10m/s$ such a representation predicts a much more rapid increase in C_{DN} than is supported by data, including those used by Garratt (1977) and Fig. 3. More recently, Smith (1988) suggested adding the two z_o expressions (35) and (36), although there is no evidence that addition is the physically correct operation:

$$z_o \;=\; \alpha_s \;\nu\; u^{*-1} + \alpha_c \;g\; u^{*2}. \tag{37}$$

In contrast, manipulating (34) leads to an exponential dependence:

$$z_o \;=\; 10m \; e^{u^*/(\kappa \; U_N)} \;=\; 10m \; e^{\sqrt{C_{DN}}/\kappa} \; . \tag{38}$$

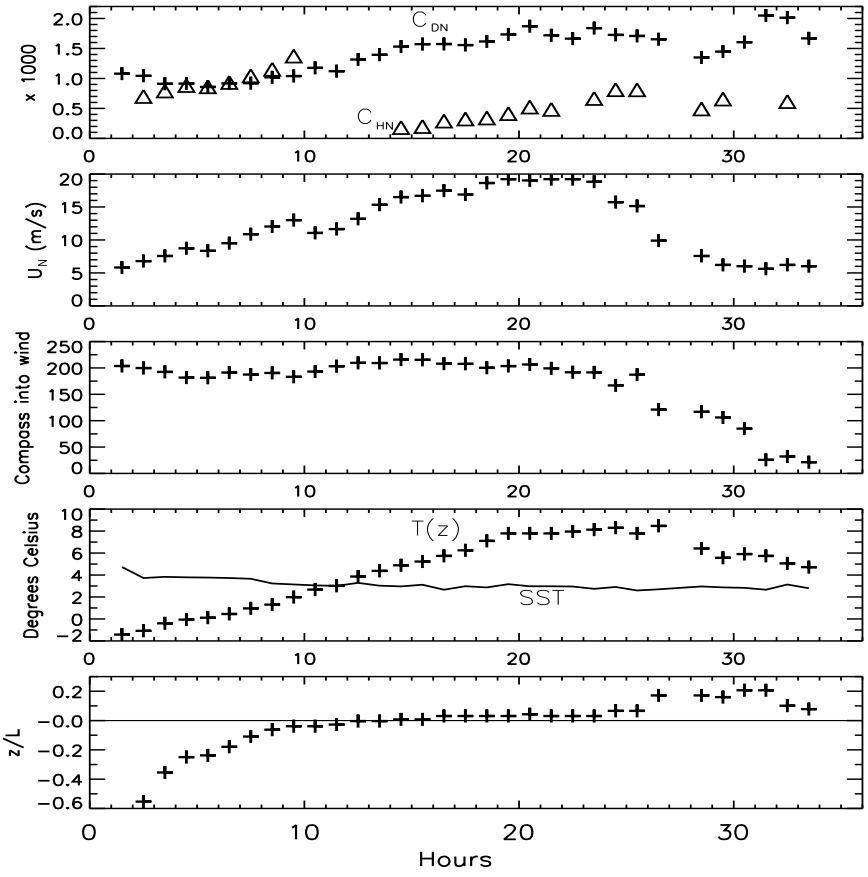

Figure 4. Time series of transfer coefficients C_{DN} (top panel pluses) and C_{HN} (top panel triangles) and corresponding wind speed, wind direction, air temperature, SST and stability (z/L).

All large data sets of measured C_{DN} display considerable scatter at any given wind speed, but the standard deviations of Fig. 3 show that

Fetch (km)	Data hours	Mean	Standard deviation	Minimum	Maximum
10 - 20	200	1.14	.18	.75	2.03
20 - 100	54	1.10	.22	.73	1.87
100 - 200	85	1.13	.24	.64	1.76
unlimited	291	1.14	.21	.62	1.75
all	590	1.13	.21	.62	2.03

Table 2. Fetch dependency of the neutral 10m drag coefficient C_{DN} for winds between 4 and 10m/s.

it tends to be greater at wind speeds below about $10m/s$. However, an error analysis suggests only about $\pm$ 20% of this can be attributed to the measurements. The remainder appears to be directly related to varying wind/wave conditions, which underlines the inadequacy of (36). This position is supported by the time series of drag coefficient measurements shown in Fig. 4. During the period of approximately steady winds between hours 15 and 24, the drag coefficient measurements display little variability, suggesting that relatively invariant coefficients may be obtained for equilibrated wind/wave conditions. However, comparing the coefficients less than 0.001 (hours 3 to 8), with those greater than 0.002 (hours 31 to 33) for similar moderate wind speeds, suggests that the latter result from the rapid decrease in wind speed and reversal of wind direction. However, when observations over many storms and frontal passages are grouped according to the wind behavior the effect is measurable, but not large. Figure 3 shows only about a 10% increase in observed C_{DN} when winds have rapidly decreased and/or changed direction over periods of rising and/or steady winds.

Quantification of other wave effects has proved elusive. Table 2 shows that between 4 and 10m/s, C_{DN} does not depend strongly on fetch, nor, by implication, on wave parameters that do, such as amplitude and wavelength. However, the ratio of these two parameters is the wave steepness which is independent of fetch, and a C_{DN} dependency is consistent with observed higher values in shallow water (steep) wave regimes.

It is interesting to note that historically, formulations of heat and moisture coefficients have more closely followed (33), which is rarely used to formulate the drag coefficient. Specifically, measured fluxes $u^*\ \theta^*$ and $u^*\ q^*$ have been regressed on $U_N\ \theta_N$ and $U_N\ q_N$, respectively. In the case of moisture, the offset is not significantly non-zero, so the slope gives C_{EN} directly from (31). However, in the heat flux case there is a significant positive offset, and furthermore, the slope is found to be steeper in unstable conditions ($u^*\ \theta^* > 0$), than in stable. Thus,

it is necessary to treat stable and unstable heat fluxes separately. The positive offset is consistent with an unbounded transfer coefficient (slope) as wind speed approaches zero, but the flux, as in the case of (8), should diminish. This behavior can also be achieved by combining (29) and (31), then using fluxes to compute the roughness lengths from

$$\frac{\kappa}{ln(10m/z_\theta)} = \frac{1}{\sqrt{C_{DN}}} \frac{u^*\ \theta^*}{\theta_N\ U_N} \ ; \tag{39}$$

$$\frac{\kappa}{ln(10m/z_q)} = \frac{1}{\sqrt{C_{DN}}} \frac{u^*\ q^*}{q_N\ U_N} \ . \tag{40}$$

Empirically, (39) is found to average about 0.0180 in stable conditions and 0.0327 in unstable, while a typical value of (40) is about 0.0346. There is relatively little scatter in these values, because of the observed variability in measured C_{HN} and C_{EN} accounted for in the drag coefficient on the right hand sides of (39) and (40). Once determined they directly give the formations of C_{HNu} (unstable), C_{HNs} (stable) and C_{HE} shown in Fig. 5.

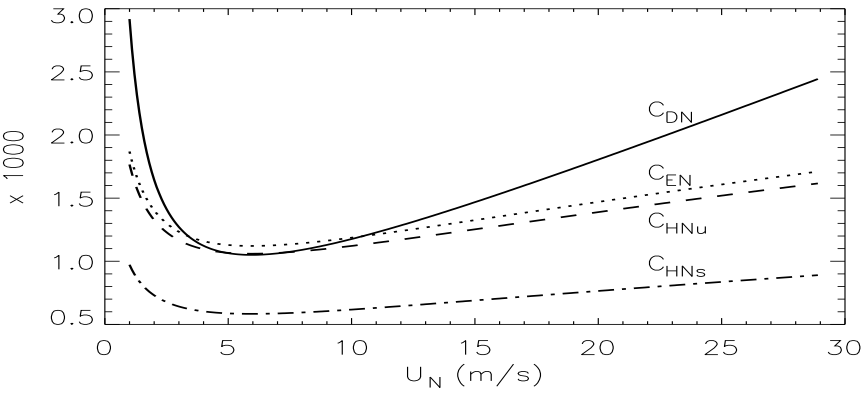

Figure 5. Neutral 10m transfer coefficients as a function of equivalent neutral 10m wind speed; C_{DN} from Eq. (34) (solid curve), C_{EN} from Eqs. (40) and (34) (dotted curve), and unstable C_{HNu} (dashed) and stable C_{HNs} (dot-dashed) from Eqs. (39) and (34).

A dramatic illustration of the effect of stability on C_{HN} is the decrease by more than a factor of two in Fig. 4 (triangles) between hours 10 and 14. During this time the increasing air temperature surpassed the SST, causing the stability parameter to change sign. The indications are that the change is abrupt at $\zeta = 0$, with high values persisting in the earlier near neutral, but still unstable conditions. The effect is smaller in the mean, but still considerable, with the 1.8 the ratio of 0.0327 to 0.0180.

Otherwise, the slow changes in C_{HN} generally follow the evolution of C_{DN}, as expected from (29) and Fig. 5.

4.1 Bulk flux estimates

Estimating the turbulent fluxes from average atmospheric and sea surface properties is essentially the inverse of determining transfer coefficients, and accordingly the bulk formulae are the inverse of (27):

$$\vec{\tau} \;=\; \rho\, C_D\, |\Delta\vec{U}|\, \Delta\vec{U}, \tag{41}$$

$$Q_H \;=\; \rho\, c_p\, C_H\, (\theta(z_\theta) - SST)\, |\Delta\vec{U}| \tag{42}$$

$$E \;=\; \rho\, C_E\, (q(z_q) - q_{sat}(SST))\, |\Delta\vec{U}| \tag{43}$$

$$Q_E \;=\; \Lambda\, E \tag{44}$$

where $\Delta\vec{U} = \vec{U}(z_u) - \vec{U}_0$. The mean wind, $\vec{U}(z_u)$, potential air temperature, $\theta(z_\theta)$, and specific humidity, $q(z_q)$, may be from different heights, z_u, z_θ and z_q, respectively. The surface current is often, but not always, negligible relative to the wind. A constant density, $\rho \approx\ 1.22 kg/m^3$ may be sufficient, but a more accurate expression is

$$\rho \;=\; \frac{P_o}{R_{gas}\, \theta(z_\theta)\, (1. + .608\; q(z_q))}, \tag{45}$$

where $R_{gas} = 287.04 J/kg/K$ is the gas constant for dry air. The order 1% effects of temperature on Λ and of humidity on c_p are usually ignored.

Although it is clear that a skin temperature should be used to compute the longwave radiation (7), a definitive study has not been conducted to determine whether a skin or bulk SST is more appropriate for (42). At present the determining factor is to use the same temperature as was used to compute C_H, which is usually a bulk temperature, because skin temperature is a very difficult measurement. This becomes an issue when satellite estimates of skin SST are available. In (43), the air at the sea surface is assumed to be saturated, with a specific humidity given well enough by

$$q_{sat}(SST) =\; 0.98\; \rho^{-1}\;\; 640380 kg/m^3\; e^{(-5107.4K/SST)}, \tag{46}$$

where the factor 0.98 applies only over sea-water. The saturation assumption has not been verified, but since it is used in formulating C_E, it should be applied in the inverse (43). The exact relation between evaporation and surface latent heat flux (44), depends on the fact that the latent heat required to evaporate comes from the liquid (the ocean). In the case of evaporation from spray this still holds unless droplets entirely

evaporate or are suspended and there is effectively a latent cooling of the lower atmosphere. The significance of this effect remains outstanding because of the lack of a direct measurement standard.

Three practical ways computing the fluxes are: A) shift the wind, temperature and humidity to 10m and neutral stability so that neutral 10m coefficients can be used directly, B) shift the coefficients to the height, and stability of the atmospheric state variables. and C) shift the temperature and humidity to the height of the wind, z_u, then shift the coefficients to this height and to the atmospheric stability. The details of (C) follow, but if the atmospheric state variables are given at the same height, it just becomes equivalent to a particularly efficient version of (B). This efficiency can also be achieved by shifting the temperature and humidity to the wind height off-line. The calculations are most efficient when the wind height, z_u, equals the 10m reference height of the transfer coefficients.

The iterative procedure for (C) is as follows:
1) Assume $\theta(z_u) = \theta(z_\theta)$ and $q(z_u) = q(z_q)$ and compute the virtual potential temperature, $\theta_v = \theta(z_u)\ (1. + .608 q(z_u))$. Then make a first guess of neutral stability and $U_N = |\Delta\vec{U}|$ to give the transfer coefficients (Fig. 5). The initial turbulent scales are then computed as:

$$\begin{aligned} u^* &= \sqrt{\rho_a^{-1}\ |\vec{\tau}|} = \sqrt{C_D}\ |\Delta\vec{U}| \\ \theta^* &= \frac{Q_H}{\rho_a\ c_p\ u^*} = \frac{C_H}{\sqrt{C_D}}\ [\theta(z_\theta) - SST] \\ q^* &= \frac{E}{\rho_a u^*} = \frac{C_E}{\sqrt{C_D}}\ [q(z_u) - q_{sat}(SST)] \end{aligned} \tag{47}$$

2) Begin the iteration loop with estimates of the stability parameters $\zeta_u = z_u/L$, $\zeta_q = z_q/L$ and $\zeta_\theta = z_\theta/L$, where L is the Monin-Obukhov length (22):

$$\zeta(z) = \frac{\kappa\ g\ z}{u^{*2}}[\ \frac{t^*}{\theta_v} + \frac{q^*}{(q(z_q) + 0.608^{-1})}\ ] \tag{48}$$

For each of the these, use (20) to find the integrals of the dimensionless flux profiles of momentum, $\psi_m(\zeta)$, and of heat and moisture, $\psi_s(\zeta)$.
3) Shift the wind speed to $10m$ and neutral stability, and the temperature and humidity to the wind height :

$$U_N(10m) = |\Delta\vec{U}|\ \ (1 + \frac{\sqrt{C_D}}{\kappa}[ln(z_u/10m) - \psi_m(\zeta_u)]\ )^{-1} \tag{49}$$

$$\theta(z_u) = \theta(z_\theta) - \frac{\theta^*}{\kappa}\ [ln(\frac{z_\theta}{z_u}) + \psi_h(\zeta_u) - \psi_h(\zeta_\theta)] \tag{50}$$

$$q(z_u) \;=\; q(z_q) \;-\; \frac{q^*}{\kappa}\,[ln(\frac{z_q}{z_u}) + \psi_h(\zeta_u) - \psi_h(\zeta_q)] \quad . \tag{51}$$

4) Update the neutral 10m transfer coefficients (Fig. 5), then shift them to the measurement height, z_u, and stability, ζ_u, using:

$$\begin{aligned} C_D(z_u,\zeta) &= C_{DN}(1 + \tfrac{\sqrt{C_{DN}}}{\kappa}\,[ln(z_u/10m) - \psi_m(\zeta_u)])^{-2} \\ C_H(z_u,\zeta) &= C_{HN}(1 + \tfrac{C_{HN}}{\kappa\,\sqrt{C_{DH}}}\,[ln(z_u/10m) - \psi_h(\zeta_u)])^{-2} \\ C_E(z_u,\zeta) &= C_{EN}(1 + \tfrac{C_{EN}}{\kappa\,\sqrt{C_{DN}}}\,[ln(z_u/10m) - \psi_h(\zeta_u)])^{-2} \end{aligned} \tag{52}$$

5) Using these transfer coefficients, $\theta(z_u)$ from (50) and $q(z_u)$ from (51), recompute the virtual potential temperature, θ_v, and update the turbulent scales in (47).
6) Start the next iteration loop at step (2) above. Over the ocean stability is usually near neutral, and 2 iterations are all that is necessary. In very stable conditions up to five iterations may be needed. After the last iteration the fluxes are computed from the last set of turbulence scales according to (15).

Even with perfect atmospheric inputs and SST, the flux estimates are only as representative of true conditions as the bulk transfer coefficients. Figure 3 shows that after the wind speed and direction shifts the momentum (heat and moisture) flux would be underestimated by nearly a factor of 2 ($\sqrt{2}$), and overestimated early in the time series. When averaged over the 3 - 7 day synoptic period, the uncertainty should diminish as wave effects start to average out. But, because of the seasonal cycle of storms, annual averaging is probably required before the uncertainty in bulk fluxes is minimized.

5. Satellite flux estimates

Satellite retrieval products are attractive for GODAE, because of the frequent, global sampling, and the possibility of near real time delivery; continued availability notwithstanding. Over the ocean satellites have been most successful at producing wind, radiation and precipitation fields. However, these are necessarily very indirect measures, and in situ measurements, are essential for providing the calibration standard, at least at a few select locations. Therefore, the accuracy of these observations will be only briefly included below, with WGASF (2000) a more complete reference. There are schemes for estimating monthly mean latent heat flux (evaporation), but this is likely too infrequent for GODAE.

5.1 Wind stress

Satellite wind products have been derived from both passive microwave radiometers and active radars (altimeters and scatterometers), but the principal source of wind direction data is scatterometers. In situ buoy measurements of U_N have been empirically related to scatterometer backscatter, σ_o, such that the accuracy of scatterometer wind speed, U_S, can be rather good; -.3m/s bias and 1.3 rms difference (Freilich and Dunbar, 1999). Taking U_S as an estimate of U_N gives the stress directly from (31) as

$$u^{*2} = C_{DN}(U_S) \;\; U_S^2 \;\; . \tag{53}$$

But is this the best calculation? From section 4 it can be argued that any drag coefficient formulation is a representation of "average" wave conditions. There are recent formulations which purport to account for at least some wave effects, given local wave conditions, which we denote as C_{DN}(waves). Figure 4 suggests that at the same wind speed, rougher seas produce greater stress that a C_{DN}(waves) formulation should be able to capture, at least in large measure. However, the observations of Li et al. (1987) suggest that the rougher seas themselves produce more backscatter and a high satellite wind , so that in order not to account for the rough surface twice, C_{DN} as in (34) should be used in (53), as given.

5.2 Radiation

The in situ measurement of radiation both incident on and reflected from the ocean surface is essentially a direct measurement. The solar and longwave components are measured by a pyranometer and a pyrgeometer, respectively. The two instruments are similar, consisting of a blackened thermopile covered by a hemispherical dome whose transmissivity matches the desired measurement. In ideal conditions pyranometer accuracy can be excellent (2 %), but variations in the temperature of the dome can be problematic. At sea conditions are far from ideal, with platform motion a serious problem unless mitigated by use of a gimbal. Other sources of error are calibration error, contamination of the dome, so all together measurement accuracy is unlikely to be no better than 5%. Longwave radiation is naturally emitted near typical pyrgeometer temperatures, so corrections need to be applied for dome temperature and emissivity to transmissivity ratio, and for the temperature of the instrument housing. Although the thermopile is shielded by a shortwave filter, the solar radiation can be so large that even a small amount of leakage can be serious. Again measurement errors of at least 5% are expected.

Satellites derive surface radiation from measurements of incoming and outgoing radiation at the top of the atmosphere. These are generally combined with information on the atmospheric column in a radiative transfer model (RTM), with the treatment of clouds of critical importance. For example, the recent ISCCP-FD dataset (Zhang et al., 2004) contains flux profiles, every 3 hours for 18 years at 280 km spatial resolution. By improving the treatment of cloud vertical structure, revising the aerosol chemistry and water vapor profiles, and accounting for diurnal skin and air temperatures, the overall uncertainty in surface fluxes is claimed to be reduced to $10 - 15 W/m^2$. The standard of comparison is the Baseline Surface Radiation Network over land (Gilgen et al., 1995), and ship radiometers as part of the SEAFLUX project (Curry et al., 2004).

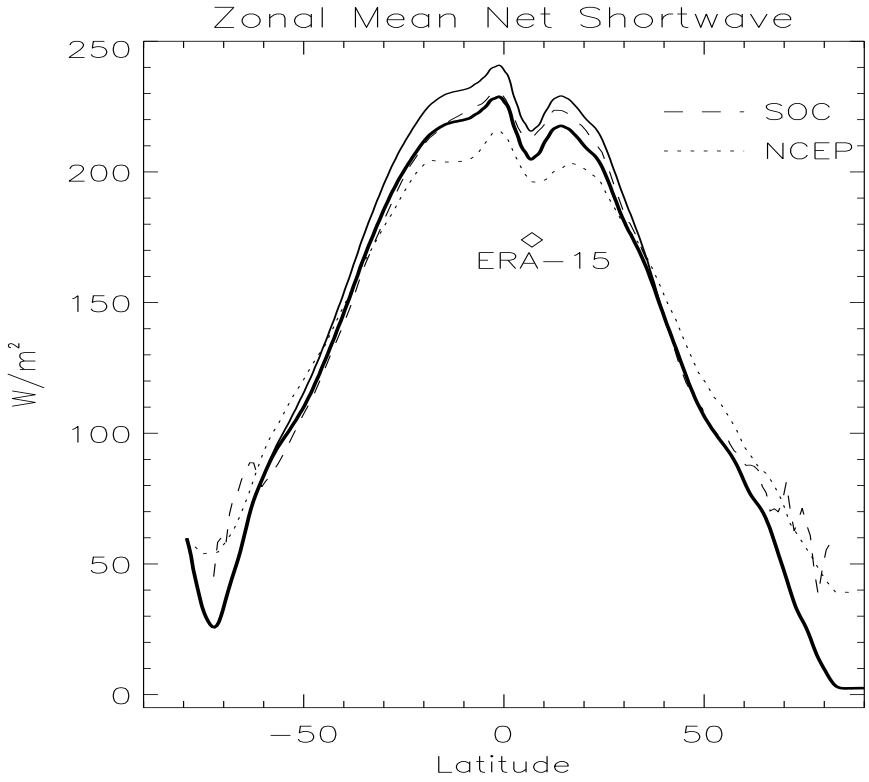

Figure 6. Zonally averaged climatological net solar radiation into the ocean from the ISCCP-FD (Zhang et al., 2004) both uncorrected (thin solid) and corrected (thick solid, see Section 6.1), compared to SOC (dashed) and NCEP reanalysis (dotted). Only one value at 5° N is shown for ERA-15.

Both Beranger et al. (1999) and WGASF (2000) compare zonal average net shortwave radiation flux from a variety of sources. Two of these (NCEP and SOC) are shown in Fig. 6 along with the ISCCP-FD product (thin solid). In the tropics, the latter is about $10 - 20 W/m^2$ greater than the Langley Research Center (Darnell et al., 1996) satellite product (not shown). There is much better agreement at higher latitudes. Although the two dataset agree to within their uncertainties, differences are significant in the tropics, where the two observational datasets, SOC (Fig. 6) and COADS (not shown) both fall about midway between the two satellite products.

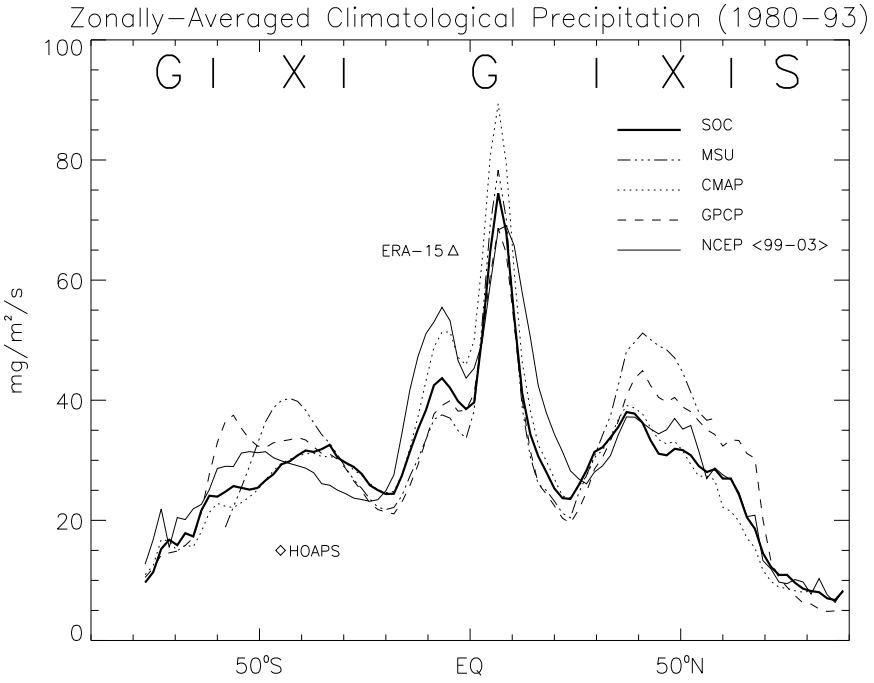

Figure 7. Comparison of zonally averaged precipitation into the ocean from a variety of climatologies.

5.3 Precipitation

The precipitation sampling problem is much less severe in satellite estimates, but the lack of accurate in situ observations makes the development and validation of algorithms difficult. Therefore, satellite precipitation data sets suitable for GODAE must be regarded as highly uncertain. Freshwater fluxes change sea surface salinity, but because these fluxes do not depend on the salinity there is no direct negative

feedback to retard the accumulation of flux error, as there is in the case of the heat flux dependence on SST. Therefore, large systematic errors are particularly problematic. The comparison of zonal averages from different precipitation data sets in Fig. 7 illustrates the problem, even though large regional differences are lost, because of compensation along latitude circles. The best agreement is found around 30° latitude in both hemispheres. Ideally, one data set would be applicable globally, but it appears that each precipitation product is demonstrably deficient in one or more of the following five zones; the Antarctic (poleward of $61°S$), the Southern ($65°S$ to $30°S$), the Equatorial ($30°S$ to $30°N$), the Northern ($30°N$ to $62°N$), and the Arctic (poleward of $62°N$).

Comparing the satellite products in the tropics, the CMAP values of Xie and Arkin (1996) are about 30% greater than GPCP (Global Precipitation Climatology Project) (Huffman et al., 1997), and more than an ocean climate model can deal with. The MSU (Microwave Sounding Unit; Spencer, 1993) falls between. In contrast, the subtropical ocean simulations are much better when forced with CMAP than either GPCP, or MSU. Polar latitudes are not sampled by some satellites, including the MSU, so CMAP becomes reliant on NWP model output, complete with spectral ringing signals in the precipitation. Therefore, the only viable Antarctic product is GPCP. It is also available in the Arctic, but doesn't compare all that well to the observed compilation of Serreze and Hurst (2000). Therefore, as denoted GXGXS in Fig. 7, a possible, but far from ideal, compromise, is to use GPCP(G), CMAP(X), GPCP(G), CMAP(X) and Serreze/Hurst(S), respectively, in the five zones noted above. Another satellite based product is HOAPS (Hamburg Ocean Atmosphere Precipitation System), but it appears to be an outlier, giving only 15 $mg/m^2/s$ at 44° S.

6. A merged flux climatology

According to WGASF (2000), "there is presently no one flux climatology which does not exhibit significant errors in one region or another in each of the various flux components." In particular, there are serious issues with the flux products from NWP reanalysis, which are also expected in the operational fluxes that would be very convenient for GODAE. Most problematic are fields like radiation and precipitation which strongly depend on the cloud field. For example, tropical radiation from NCEP (Fig. 6) is significantly lower than all satellite products, with ERA-15 producing even less solar heating. Also, NCEP precipitation (Fig. 7) around $5°S$, is much greater than other datasets, with the better agreement with CMAP due to CMAP's blending of station

	CORRECTIONS			
	NONE	WIND	HUMIDITY	ALL
$f_o\ Q_S$	173	173	173	165
$f_o\ Q_L$	-52	-52	-52	-52
$f_o\ Q_E$	-76	-84	-89	-97
$f_o\ Q_H$	-13	-14	-13	-14
$f_o(Q_{as} - Q_P)$	31	23	18	1
$f_o\ E$	-30.5	-33.4	-35.6	-39.0
$f_o\ P$	30.4	30.4	30.4	35.4
R	3.5	3.5	3.5	3.5
$f_o\ F_{as} + R$	3.4	0.5	-1.7	-0.1

Table 3. Global mean air-sea fluxes 1984–2000 and continental runoff with no correction (NONE), only the wind speed correction (WIND), only the relative humidity correction (HUMIDITY) and with all the corrections of Section 6.1 (ALL). Heat fluxes are in W/m^2, and freshwater fluxes are in $mg/m^2/s$ ($0.0864mm/day \approx 31mm/year$). If the true ocean area of $3.523 \times 10^8 km^2$ is used to divide the sum of all runoff in Fig. 1 the Runoff becomes, R = 3.574 $mg/m^2/s$, or $1.26Sv$.

and satellite rainfall with NCEP. Again, ERA-15 is even further afield. A major improvement in these NWP fields would seem to require the proper assimilation of observed cloud into NWP analyses. In principle, the accuracy of the radiative fluxes should then approach that of the off-line RTE fluxes.

WGASF (2000) recommends merging a number of different datasets in order to assemble a complete collection of surface flux data that is superior to all the individual datasets. One such example has been developed by Large and Yeager (2004) and is presented below. Their choices were made on the basis of global coverage, frequency duration and the behavior of ocean and sea-ice models. Other justifiable choices could have been made and most are discussed at length by WGASF (2000). The global NCEP/NCAR reanalysis gives the atmospheric state, the ISCCP-FP product provides the radiation fields, the precipitation is the blend of multiple products denoted (GXGXS) in Fig. 7, the continental runoff is shown in Fig. 1, the sea-ice concentration comes from the National Snow and Ice Data Center, historical SST is a reconstruction (Rayner et al. 2003) that has been made compatible with sea-ice concentration.

6.1 Empirical corrections

The most important aspect of flux dataset development is the use of other limited, but higher quality data sets to determine objective corrections to the flux data sets. The corrected/adjusted forcing is used

in conjunction with observed SST to produce an observationally based air-sea flux climatology over 43 years. A necessary achievement of the exercise is to lower the global air-sea heat flux over 17 years (1984–2000) from $31 W/m^2$ heating to a more reasonable $1 W/m^2$ (Table 3). A freshwater imbalance of $3.4 mg/s/m^2$ is over compensated by increased evaporation, so an overall increase in precipitation is used to give a nearly balance ($-0.1 mg/s/m^2$) global mean budget. The impact on these global budgets of the following corrections is summarized in Table 3.

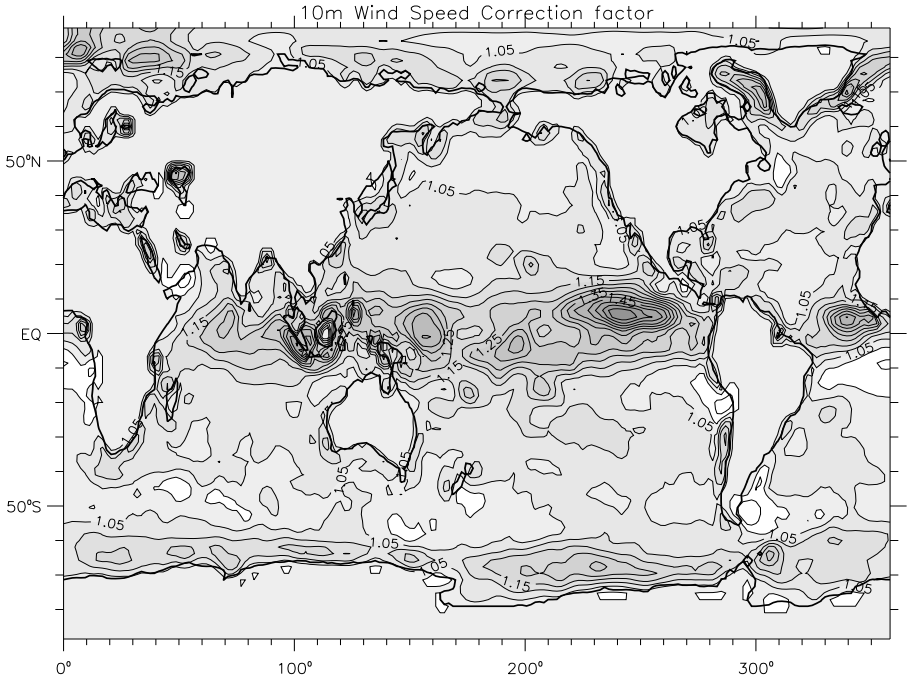

Figure 8. Ratio of two-year mean QSCAT and NCEP wind speeds. Contour interval is 0.05. Regions of weaker NCEP winds (ratio greater than 1.0) are shaded.

A recent comparison of NCEP reanalysis fields with research vessel observations shows evidence of a consistent low bias in NCEP wind speeds at all latitudes (Smith et al. 2001). The advent of satellite wind speed products makes a more global assessment possible. Physically, these speeds should best correspond to $\Delta\vec{U}$ and are a more straightforward scatterometer measurement than the wind direction. We utilize the QSCAT (QuikScat scatterometer) wind fields over a two-year period (2000-2001). These are constructed 6-hourly on a half degree grid following

Chin et al. (1998). Figure 8 shows the ratio of the two year mean QSCAT speed to that from NCEP. A low bias is evident in the NCEP winds, with this ratio greater than 1 everywhere except a few isolated (unshaded) regions off the coasts of South America and Africa. The QSCAT winds are between 5 and 10% higher than NCEP winds over most of the mid-latitude ocean, and the ratio is considerably higher in select regions near the equator and the poles. To correct the NCEP wind speed bias, both reanalysis vector wind components are multiplied by the spatially-dependent factor plotted in Fig. 8. An important effect is to make the evaporation and turbulent heat fluxes more negative, thereby improving the global heat balance by 8 W/m^2, and the freshwater balance by 2.9 $mg/m^2/s$ (Table 3).

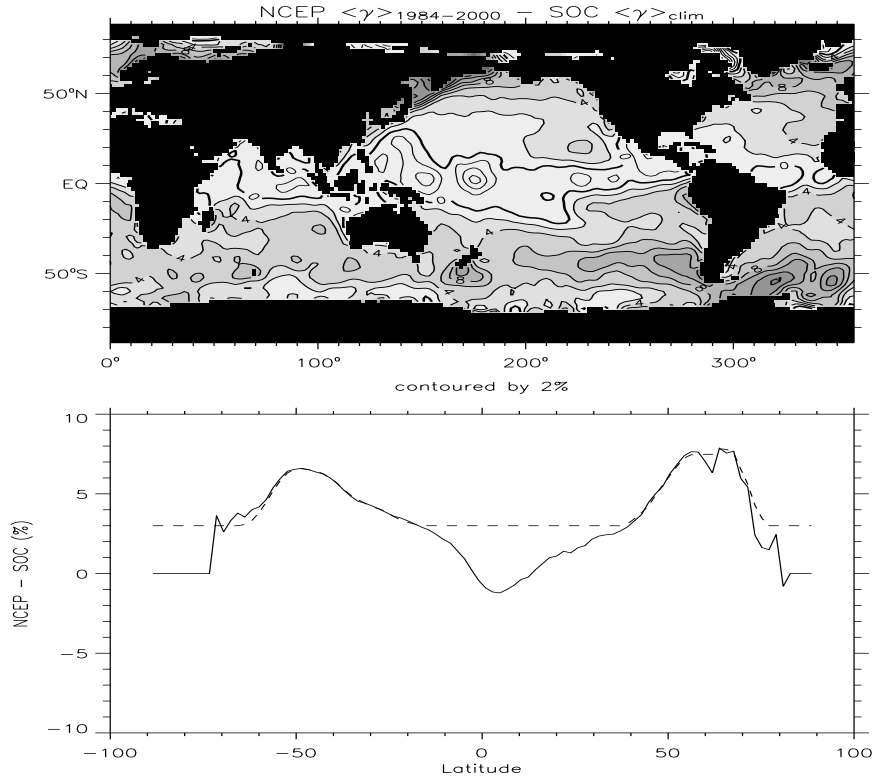

Figure 9. Comparison of NCEP/NCAR Reanalysis relative humidity with Southampton Oceanography Center (SOC) climatology as a mean difference (top panel) and as a zonally-averaged mean difference (bottom panel). Relative humidity values and differences are in %. The dashed line in the bottom panel shows the modified, smoothed version of the zonal-average difference used for correcting NCEP relative humidity as a function of latitude.

The near surface humidity in the NCEP reanalysis is too high (Fig. 9), with the relative humidity, γ, seldom less than 80%. Large et al. (1997) were able to match the Kent et al. (1993) observed annual cycle of latent heat flux in the North Atlantic only after reducing the NCEP specific humidity by a factor of 0.93. In the western tropical Pacific, a comparison of NCEP relative humidity to TAO mooring data in the equatorial Pacific shows a year-round positive bias of $\approx 2-3\%$ (Wang and McPhaden 2001). Plausible reasons for this bias are that ship based ocean humidity measurements that are assimilated into the reanalysis are more likely too wet than too dry (Kent et al. 1993), and that the NCEP model evaporates too much (Smith et al. 2001) and transports too little vertically out of the boundary layer. The excess evaporation is accomplished despite the low wind speeds and moist near surface by an excessively large C_E (Smith et al. 2001). The TAO data suggests reducing NCEP relative humidity by 3% in the tropics and this is used as a minimum correction at all latitudes. Figure 9 shows that NCEP relative humidity exceeds the SOC climatology almost everywhere outside the tropical band, with local differences exceeding 14%. The SOC humidities should be most reliable in the northern Hemisphere, because of the greater number of ship reports and the extensive work of Kent et al. (1993) in the North Atlantic. Therefore, in the north a smoothed version of the zonally averaged difference is used as a correction wherever it exceeds the minimum 3%. In the absence of any further information, and because of the rough symmetry in Fig. 9 about the equator, a similar correction is applied in the south, but with much less confidence. It is a maximum of about 6% at $50°S$. The net result is the NCEP bias $\delta\gamma$ shown as a function of latitude by the dashed line in Fig. 9. Overall, lowering the relative humidity increases the latent heat flux loss by $13W/m^2$ (Table 3).

Over most of the globe NCEP surface air temperatures are not corrected. However, comparison of NCEP temperatures with weather station and drifting buoy data from Antarctica reveals that a persistent very cold bias exists in the reanalysis product at extreme southern latitudes, especially in the winter. In the Arctic, the POLES (Polar Exchange at the Sea Surface) project has combined buoy and land station temperature data within an optimum interpolation scheme (Rigor et al., 2000). Over the Arctic cap north of $70°N$, the annual average POLES and NCEP air temperatures differ randomly by only about $\pm 0.5°C$, but NCEP air-temperatures are corrected monthly by the mean monthly climatological difference between POLES and NCEP. The 12 monthly corrections (January through December) are 0.49, 0.06, -0.73, -0.89, -0.77, -1.02, -1.99, -0.91, 1.72, 2.30, 1.81 and $1.06°C$.

Shortwave radiation is greatest at latitudes where there is a lot of ocean. Therefore, small tropical and sub-tropical errors in this field can significantly impact the global heat balance. Comparisons of Q_S such as Fig. 6, and the need to achieve a better global heat balance suggest reducing Q_I from ISCCP-FP by 5% for all latitudes from $50°S$ to $30°N$. For smoothness, the correction is linearly diminished between $50°S$ and $60°S$ and between $30°N$ and $40°N$. The resulting net shortwave, Q_S, is shown by the thick solid curve in Fig. 7. The global mean is reduced by 8 W/m^2 (Table 3).

With the above wind and humidity corrections and uncorrected GXGXS precipitation, the global ocean freshwater budget (4) is about -5 mg/m$^2/s$. To better balance the global oceanic water budget, both a gain (1.1417) and bias (0.7 mg/m$^2/s$) are applied to the GXGXS precipitation fields. The global mean freshwater flux then becomes -0.1 mg/m$^2/s$ (Table 3). This correction is designed to shift the GPCP curve of Fig. 8 into agreement with SOC and MSU at the 7° N peak in precipitation. By chance, the improved SOC agreement holds equatorward of about 35°. However, farther poleward the corrected precipitation becomes higher than SOC, but is still less than GPCP in both hemispheres, as favored by ocean model salinity results.

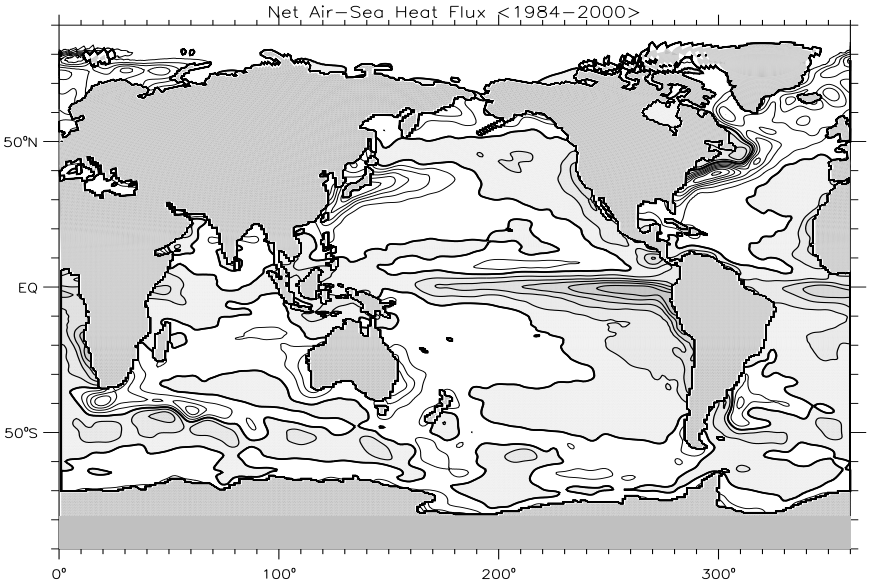

Figure 10. Climatological (1984-2000) mean total air-sea heat flux. The contour interval is 25 W/m^2, the zero contour is thicker and shaded regions indicate positive net flux into the ocean. A 5x5-point boxcar smoother has been applied twice after a uniform subtraction of the global mean imbalance of ≈ 1 W/m^2.

6.2 The mean flux fields and balances

The ocean surface fluxes forcing any GODAE system should not only produce mean net fields comparable to climatologies, but the component balances should also be similar. Significant departures may be indicators of errors in the data and/or the model. The climatological mean air-sea heat flux ($f_o\, Q_{as}$) computed from 1984 through 2000 is shown in Fig. 10. All the expected features are evident; strong heating along the equator with a maximum in the eastern Pacific in excess of $125 W/m^2$, a band of predominant heating along $50°S$, heating along the eastern boundaries of the subtropical gyres of the Pacific and Atlantic, strong cooling in the Nordic seas between Greenland and Europe and between Greenland and Labrador, and strong cooling over the western boundary currents and their extensions, including the Agulhas retroflection. The uncertainties in all fluxes climatologies means that there are always similarities and differences in detail. However, one large scale difference between Fig. 10 and the SOC climatology is the much greater SOC heating in the tropics from Africa east to the dateline. The area is great enough to factor significantly in the SOC global heat imbalance of $30 W/m^2$. It includes the TOGA COARE region of the western Pacific where SOC shows $60 W/m^2$ heating compared to less than $25 W/m^2$. Ocean budget (e.g. Gent, 1991) and observational estimates place the net heat flux at between 10 and $20 W/m^2$.

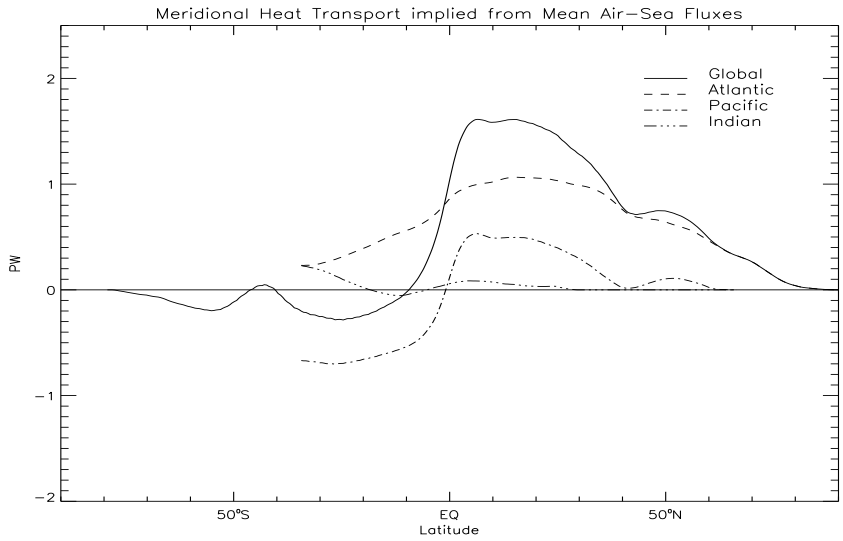

Figure 11. Implied meridional heat transport from the Fig. 10 heat flux.

Figure 11 shows the northward heat transport (global and by basin) implied by the air-sea heat fluxes of Fig. 10. In such a plot, the zonal average heat flux gives the slope of the curves (positive for heating, negative for cooling), while the value at a particular latitude represents the integrated heat flux from all ocean areas farther north, or equivalently in a balanced system, minus the integrated heat flux from all ocean areas farther south. The missing ocean heat loss via ice-ocean fluxes are believed to be only few W/m^2, but these would steepen the negative slopes at high latitudes and give larger poleward maxima in both hemispheres. Figure 11 suggests that the heating around $50°S$ is approximately equal to all the heat loss farther poleward, so that very little heat is transported across $40°S$. Similarly, there is little transport across $10°S$, because of nearly equal, but opposite transports in the Pacific and Atlantic. Note that the sum of Indian plus Pacific transport gives the correct Indo-Pacific implied transport, but partitioning between the two basins assumes no heat transport via the Indonesian Throughflow, which is not correct.

Figure 12 shows the mean (1984 – 2000) global distribution of air-sea freshwater flux (1984 – 2000), plus the climatological continental runoff from Fig. 1. The obvious freshwater source regions (unshaded in Fig. 12) are the intertropical convergence zones (ITCZs), the mid-latitude storm tracks of both hemispheres, and the mouths of large rivers. There is net water loss (evaporation) from the Arabian Sea and the subtropical gyres of each ocean basin. These features are common to all freshwater flux climatologies, although the magnitudes of the precipitation and evaporation differ substantially, with no way of determining reality. The zonal averages of the freshwater flux and its components are shown in Large and Yeager (2004). The runoff is most significant where Siberian rivers discharge between 60 and $70°N$.

Integration of fluxes in Fig. 12 gives the implied northward transport of freshwater shown in Fig. 13. Again partitioning between the Indian and Pacific incorrectly assumes no transport through the Indonesian Throughflow. The total transport can be compared to several other estimates and direct observations given be (Wijffels, 2001). In general there is better agreement with the direct observations in the northern Hemisphere than in the southern.

Climatologies (1984 – 2000) of the zonal and meridional wind stress components are shown in Fig. 14. The pattern and magnitudes of both components are remarkably similar to the SOC climatology, which has generally larger stress magnitudes than the COADS (Beranger, 1999). Since the SOC and COADS are based on essentially the same ship observations this difference is likely due to use of a different drag coefficient

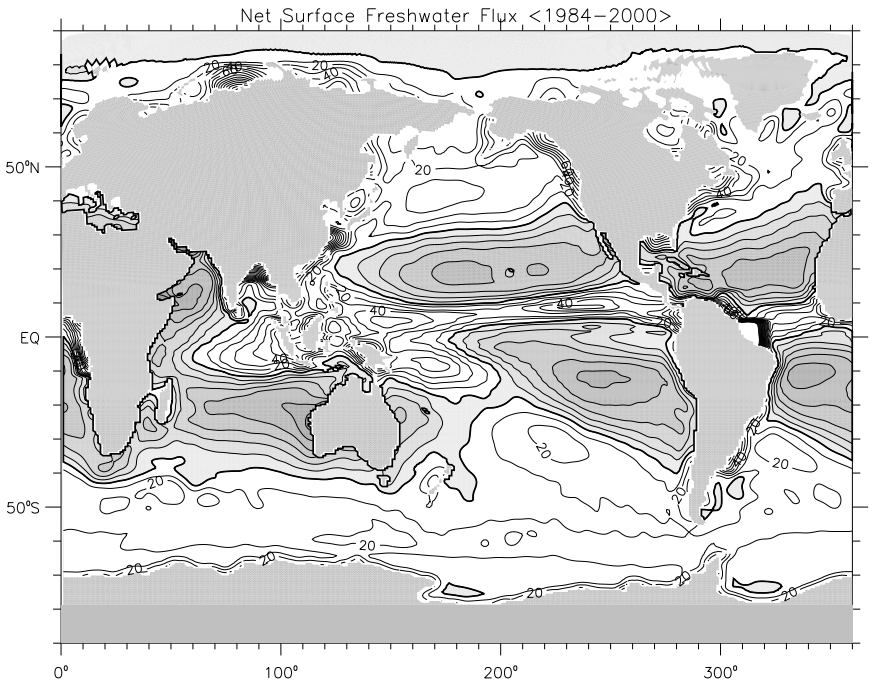

Figure 12. Climatological (1984-2000) mean total air-sea freshwater flux. Contour interval is 10 $mg/s/m^2$, up to ±100. Unshaded regions indicate positive net water flux into the ocean. A boxcar smoother has been applied twice.

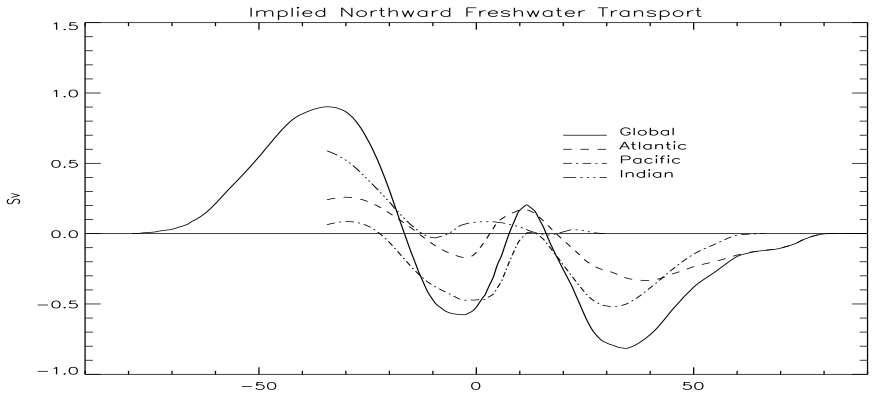

Figure 13. Implied meridional freshwater transport from the Fig. 12 freshwater flux.

formulation. It also appears that NCEP reanalysis employs a larger drag coefficient than Eq. (35), because a comparison (not shown) of NCEP stress and Fig. 14 does not show the differences implied by the wind speed correction of Fig. 8.

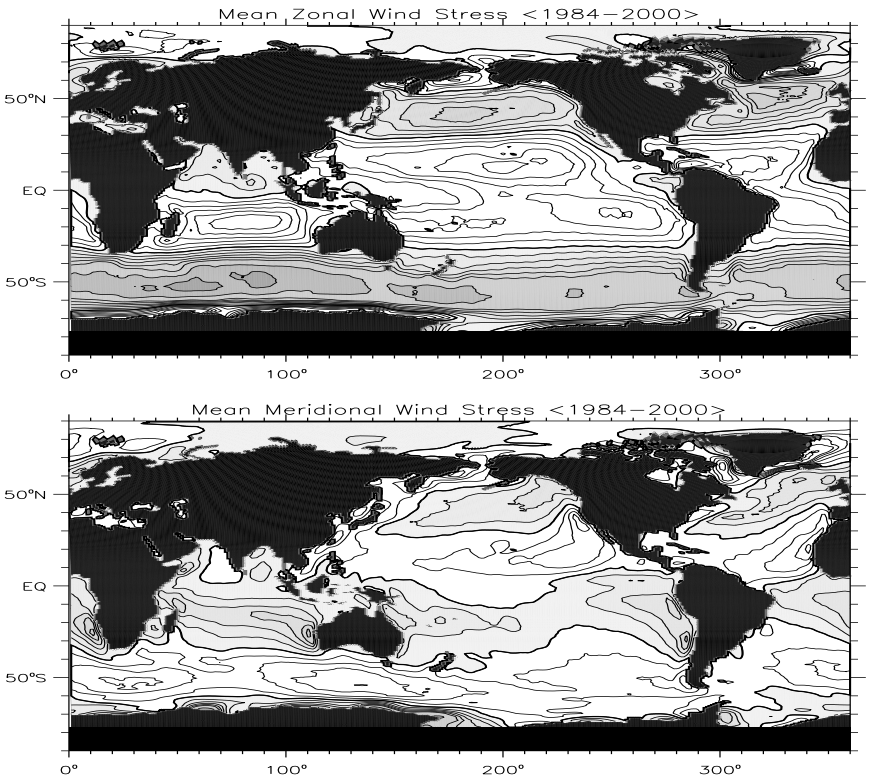

Figure 14. Climatological (1984-2000) mean zonal wind stress (top) and mean meridional wind stress (bottom) in N/m^2. Contour intervals are $\pm$(.02,.04,.06,.08,.1,.15,.2,.3) with a thick contour at 0. Positive (eastward and northward) stress values are shaded.

6.3 Interannual variability

Much of the observed interannual to decadal climate variability is displayed in Fig. 15, as time series of several large scale indices from 1950 - 2000. The North Atlantic Oscillation (NAO) and North Pacific (NP) indices are winter averages of December through March and November through March, respectively, but are plotted at mid-year. The El Nino - Southern Oscillation (ENSO) signals are the SST Anomaly from the Nino 3.4 region and the Southern Oscillation Index. These values and the Antarctic Oscillation (AAO) are 5 month running means of monthly values. All the indices display significant interannual and longer variability, that should also be prominent in incremented GODAE fluxes.

Large and Yeager (2004) computed annual means of all the fluxes for the 43 years from 1958 through 2000. On these time scales, different air-

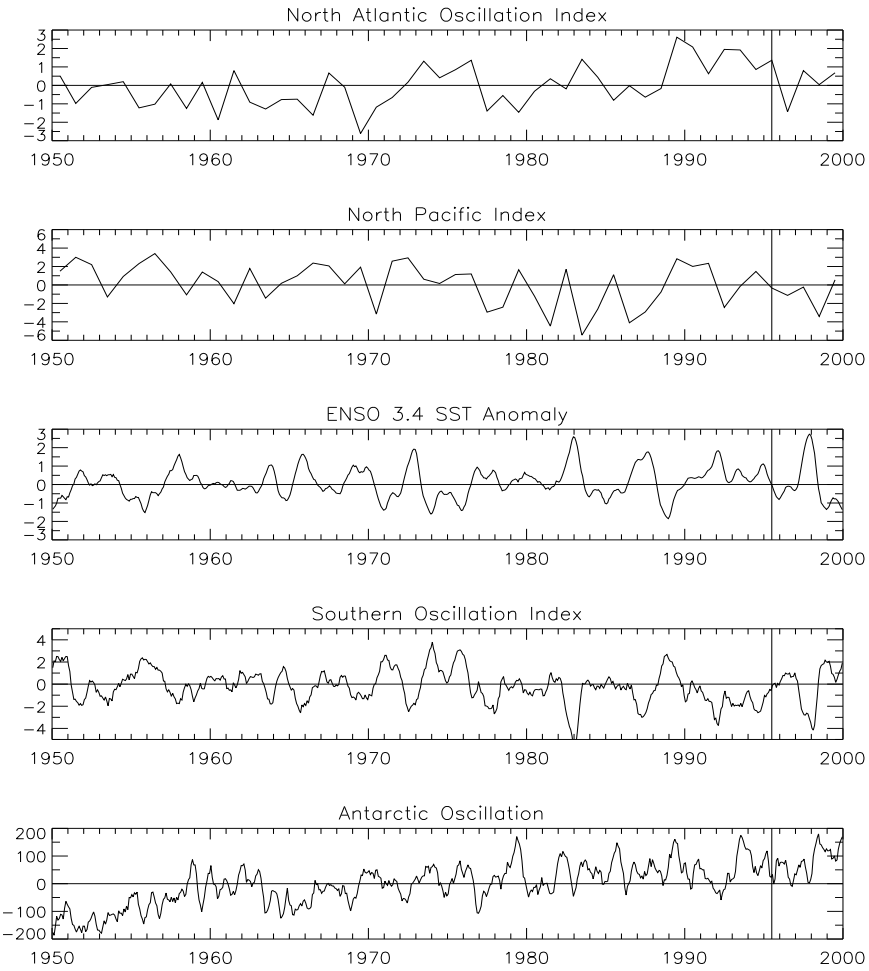

Figure 15. Interannual variability (1950 - 2000) of large scale climate indices.

sea interaction processes may be at work in the different ocean basins, so after removal of the climatological means, they constructed zonally averaged flux anomalies for the Indian, Pacific and Atlantic Oceans. An important caveat is that only the atmospheric state and SST datasets vary throughout the 43 years. Other dataset have been extended back in time using climatological annual cycles of monthly means from the period of time for which they are available. There is no variability in runoff.

The full variability of zonally averaged annual air-sea heat flux anomalies after 1983 is not noticeably different than the earlier partial variability, suggesting that the radiation does not contribute much to interan-

nual variability even though it dominates the seasonal cycle. This notion is confirmed by the annual anomalies of Q_S. The maximum anomaly is only $-10W/m^2$. It is evident in 1992 between the equator and $20°S$ in the Pacific and Atlantic Oceans, and to a lesser extent in the Indian. This signal appears to be mostly a response to the Pinatubo volcanic eruption of late 1991. The interannual variability of the air-sea freshwater flux is dominated by fluctuations in tropical precipitation. Therefore, the interannual variability of freshwater forcing prior to the satellite era remains obscure, because the dominant signal is missing.

The interannual AAO variability is most clearly reflected in the zonal wind stress anomalies south of $40°S$ in all three basins, but especially the Indian ocean. In particular, weaker eastward stress in the 1960s corresponds to negative AAO, while the large positive AAO peaks in 1979, 1985, 1989, 1993 and 1998 are all associated with positive wind stress anomalies. Meridional anomalies are weaker, but positive northward wind stress anomalies tend to be associated with negative AAO (e.g. the 1960s). Interestingly, the changing winds are not consistently reflected in the heat flux anomalies.

El Nino/Southern Oscillation (ENSO) variability is reflected in the dominant tropical precipitation signals, with annual mean anomalies from years following warm events being strongly positive in the Pacific, weakly positive in the Indian, and negative in the Atlantic. The heat fluxes have a corresponding signal only in the Pacific where they respond directly to warmer SST by becoming more upward (negative). Thus, they retard ENSO warming and cooling, as they do in a forced ocean hindcast (e.g. Doney et al., 2003).

Zonal wind stress anomalies, and to a lesser extent meridional anomalies in the North Atlantic poleward of about $40°N$ reflect the North Atlantic Oscillation (NAO), with positive stress when the NAO index is high. Corresponding negative heat flux anomalies (more latent and sensible cooling when the westerly winds are stronger) are evident, but less pronounced during the period of generally high NAO index during the 1990s.

Neither the heat flux, nor wind stress anomalies in the North Pacific appear to be directly related to the North Pacific Index (NPI). Low values of the index correspond to both positive (e.g. 1970) and negative (e.g. 1981 and 1983) zonal stress variations. The heat flux anomalies tend to follow the wind and are, therefore, of the opposite sign. There is no persistent anomaly in either the heat flux, or zonal stress through the period of high NPI from 1989 through 1991.

7. Discussion and conclusion

The uncertainties in air-sea fluxes are difficult to quantify, with the lack of direct measurements a major problem, but they decrease as the time and space scales expand. Best known are the global, long term mean heat and freshwater fluxes, which ocean inventories show are near zero. At the other extreme are turbulent fluxes whose sign at a point can be uncertain on time scales less than about 10 minutes. Perhaps most relevant to GODAE are hourly fluxes on a spatial scale of 10 km or more. Some of these might be tractable from satellite measurements, but whenever bulk aerodynamic formulae are involved there is at least a factor of 2 uncertainty due to transfer coefficient variability on these scales.

The temptation for GODAE to simply utilize global fields of Q, F and wind stress should be resisted, because too much good physics is lost. Notable examples include the penetration of solar radiation into the upper ocean, the relationship between evaporation and the latent heat flux, sea-ice coverage and the strong dependence of fluxes on SST. However, the price is high because of the large number of forcing fields necessary to prescribe the flux components.

Unfortunately, there is no single flux data suitable for GODAE. Instead, various data sets should be merged within an assimilation data stream. However, a crucial procedure within the stream should be the correction of most fields for known biases, as revealed by comparisons with more limited, but more accurate and better understood observations. These adjustments should result in global heat and freshwater fluxes that are nearly in balance, and these budgets should not be overly upset by any increments made to the fluxes during the assimilation cycle. In addition the incremented fluxes ought to display the observed features of global variability, especially those portrayed by large scale climate indices.

The forcing of a truly global ocean data assimilation system that incorporates all the details of the known physics would be extremely complicated. Therefore, simplifications should be sought, but implemented only if well understood and demonstrated to be tolerable from the viewpoint of assimilation products. A prime example is high latitude forcing where representation of much of the physics requires a coupled sea-ice model. Another is forcing near coastlines, where some satellite products are contaminated by the land and continental runoff is complicated. Also, some fluxes may not need to be accounted for; such as the temperature of precipitation and runoff, the latent heat of fusion of glacier and ice-sheet runoff, and the melting of snow.

References

Baumgartner, A. and E. Reichel, 1975: The World Water Balance. Elsevier, New York, 180pp.

Beranger, K., K. Viau, B. Barnier, E. Garnier, J. M. Molines, and L. Siefridt, 1999: An atlas of climatic estimates of air-sea fluxes. MEOM, Laboratoire des Ecoulements Geophysiques et Industriels, Institute de Mechanique de Grenoble, 19pp + figures.

Bradley, E.F. A shearing stress meter for micro-meteorological studies. *Quart. J. Roy. Met. Soc.*, **94**, 380-387.

Busch, N.E., 1977: Fluxes in the surface boundary layer over the sea. Modelling and Prediction of the Upper Layers of the Oceans, E.B. Krauss (ed.), Pergamon Press, Oxford, 72–91.

Charnock, H., 1955: Wind stress on a water surface. *Quart. J. Roy. Met. Soc.*, **81**, 639–640.

Chin, T.M. R.F. Milliff and W.G. Large, 1998: Basin-scale high-wavenumber sea surface wind fields from multiresolution analysis of scatterometer data. *J. Atmos. Oceanic Technol.*, **15**, 741–763.

Curry, JA., A. Bentamy, M.A. Bourassa, D. Bourras, E.F. Bradley, M. Brunke, S. Castro, S.H. Chou, C.A. Clayson, W.J. Emery, L. Eymard, C.W. Fairall, M. Kubota, B. Lin, W. Perrie, R.A. Reeder, I.A. Renfrew, W.B. Rossow, J. Schulz, S.R. Smith, P.J. Webster, G.A. Wick and X. Zeng, 2002: Seaflux. *Bull. Amer. Meteor. Soc.*, **85**, 409–424.

Darnell, W.L., W.F. Staylor, N.A. Richey, S.K. Gupta and A.C. Wilber, 1996: Surface radiation budget: A longterm global dataset of shortwave and longwave fluxes. *Eos, Trans. Amer, Geophys. Union.* February.

da Silva, A., C. Young and S. Levitus, 1994: Atlas of surface marine data 1994. NOAA Atlas NESDIS 6. (6 volumes), U.S. Dept. of Commerce, NODC, User services branch, NOAA/NESDIS/E/OC21.

Deacon, E.L., 1973: Geostrophic drag coefficients. *Boundary-Layer Meteorol.*, **5**, 321–340.

Doney, S.C., S.G. Yeager, G. Danabasoglu, W.G. Large and J.C. McWilliams, 2003: Modeling global oceanic interannual variability (1958-1997): Simulation design and model-data evaluation. NCAR Tech. Note, TN-452+STR, 48pp.

Fekete, B.M., C.J. Vorosmarty and W. Grabs, 1999: An improved spatially distributed runoff data set based on observed river discharge and simulated water balance. Complex Systems Research Center, U. New Hampshire.

Freilich, M.H. and R.S. Dunbar, 1999: On the accuracy of the NSCAT 1 vector winds: Comparisons with National Data Buoy Center buoys. *J. Geophys. Res.*, **104**, 11231–11246.

Fung, I.Y., D.E. Harrison and A.A. Lacis, 1984: On the variability of the net longwave radiation at the ocean surface. *Rev. of Geophys.*, **22**, 177–193.

Garratt, J.R., 1977: Review of drag coefficients over the oceans and continents. *Mon. Weather Rev.*, **105**, 915–929.

Gent, P., 1991: The heat budget of the TOGA-COARE domain in an ocean model. *J. Geophys. Res.*, **96**, 3323–3330.

Gibson, J.K., P. Kallberg, S. Uppala, A. Hernandez, A. Nomura and E. Serrano, 1997: ECMWF re-analysis project, 1. ERA description. ECMWF, Project Report Series.

Gilgen, H.C., C.H. Whitlock, F. Koch, G. Mueller, A. Ohmura, D. Steiger and R. Wheeler, 1995: Technical plan for Baseline Surface Radiation Network (BSRM) Data Management. WCRP, WMO TD-No. 443, WMO, Geneva.

Haugen, D.A, J.C. Kaimal and E.F. Bradley, 1971: An experimental study of Reynolds stress and heat flux in the atmospheric surface layer. *Quart. J. Roy. Met. Soc.*, **97**, 168-180.

Högström, U., 1988: Non-dimensional wind and temperature profiles in the atmospheric surface layer: A re-evaluation. *Boundary-Layer Meteorol.*, **42**, 55–78.

Huffman, G.R., R.F. Adler, P. Arkin, A. Chang, R. Ferraro, R. Gruber, J. Janowiak, A. McNab, B. Rudolf and U. Schneider, 1997: The global precipitation climatology project (GPCP) combined precipitation data set. *Bull. Amer. Meteor. Soc.*, **78**, 5-20.

Josey, S., C.E. Kent and P.K. Taylor, 1998: The Southampton Oceanography Centre (SOC) ocean-atmosphere heat, momentum and freshwater flux atlas. Report No.6, Southampton Oceanography Centre, 30pp.

Kalnay, E., M. Kanamitsu,R. Kistler, W. Collins, D. Deaven, L. Gandin , M. Iredell, S. Saha, G. White, J. Woollen, Y. Zhu , M. Chelliah, W. Ebisuzaki , W. Higgins, J. Janowiak, K.C. Mo, C. Ropelewski , A. Leetmaa, R. Reynolds and R. Jenne, 1996: The NCEP/NCAR 40-Year reanalysis project. *Bull. Amer. Meteor. Soc.*, **77**, 437–471.

Kent, E.C., P.K. Taylor, B.S. Truscott and J.S. Hopkins, 1993: The accuracy of voluntary observing ships' meteorological observations: Results of the VSOP-NA. *J. Atmos. Oceanic Technol.*, **10**, 591–608.

Knox, J.L., 1991: An assessment of the 27-year record of measured precipitation at Ocean Weather Station "P" in the northeast Pacific Ocean. *Clim. Bull. Canadian. Met. Ocean. Soc.*, **25**, 65–80.

Large, W.G. and S. Pond, 1981: Open ocean momentum flux measurements in moderate to strong winds. *J. Phys. Oceanogr.*, **11**, 324–336.

Large, W.G. and S. Pond, 1982: Sensible and latent heat flux measurements over the ocean. *J. Phys. Oceanogr.*, **12**, 464–482.

Large, W.G., G. Danabasoglu, S.C. Doney and J.C. McWilliams, 1997: Sensitivity to surface forcing and boundary layer mixing in a global ocean model: Annual-mean climatology. *J. Phys. Oceanogr.*, **27**, 2418–2447.

Large, W.G. and S.G. Yeager, 2004: Diurnal to decadal global forcing for ocean and sea-ice models: The data sets and flux climatologies. NCAR Technical Note, NCAR/TN-460+STR, 105pp.

Levitus, S., T. Boyer, M. Conkright, D. Johnson, T. O'Brien, J.Antonov, C. Stephens and R. Gelfeld. World ocean database 1998. NOAA, NESDIS Atlas.

Levitus, S., J. I. Antonov, T. P. Boyer and C. Stephens, 2000: Warming of the World Ocean. *Science*, **287**, 2225–2229.

Li, F., W.G. Large, W. Shaw, E. Walsh, and K. Davidson).1989: Ocean radar backscatter relationship with near surface winds: A case study during FASINEX. *J. Phys. Oceanogr.*, **19**, 342-353.

Lind, R. and K. Katsaros, 1986: Radiation measurements and model results from R/V Oceanographer during STREX 1980. *J. Phys. Oceanogr.*, **91**, 13308–13314.

Lumley, J.L. and H.A. Panofsky, 1964: The Structure of Atmospheric Turbulence. Interscience, New York, 239pp.

Paulson, C.A., 1970: Representation of wind speed and temperature profiles in the unstable atmospheric surface layer. *J. Appl. Meteorol.*, **9**, 857–861.

Payne, R.E., 1972: Albedo of the sea surface. *J. Atmos. Sci.*, **29**, 959–970.

Perry, G., P.B. Duffy and N.L. Miller, 1996: An extended data set of river discharges for validation of general circulation models. *J. Geophys. Res.*, **101**, 21339–21349.

N.A. Rayner, D.E. Parker, E.B. Horton, C.K. Folland, L.V. Alexander and D.P. Powell, 2003, Global analyses of SST, sea ice and night marine air temperature since the late nineteenth century. *J. Geophys. Res.*, **108**, 4407.

Rigor, I., R. Colony and S. Martin, 2000: Variations in surface air temperature observations in the Arctic 1979–97. *J. of Climate*, **13**, 896–914.

Roll, H.V., 1965: Physics of the Marine Atmosphere. Academic Press, 426pp.

Schmidt, G.A., C.M. Bitz, U. Mikolajewicz and L.B. Tremblay, 2004: Ice-ocean boundary conditions for coupled models, *Ocean Modelling*, **7**, 59–74.

Serreze, M.C., and C.M. Hurst, 2000: Representation of mean Arctic precipitation from NCEP-NCAR and ERA reanalyses. *J. of Climate*, **13**, 182–201.

Smith, S. and F.W. Dobson, 1984: The heat budget at Ocean Weather Station Bravo. *Atmos. Oceans*, **22**, 1-22.

Smith, S.R., D. M. Legler and K. V. Verzone, 2001: Quantifying uncertainties in NCEP reanalyses using high-quality research vessel observations *J. of Climate*, **14**, 4062–4072.

Spencer, R.W., 1993: Global oceanic precipitation from the MSU during 1979-91 and comparisons to other climatologies. *J. of Climate*, **6**, 1301–1326.

Stammer, D., C. Wunsch, R. Giering, C. Eckert, P. Heimbach, J. Marotzke, A. Adcroft, C.N. Hill and J. Marshall, 2002: The global ocean circulation during 1992-1997, estimated from ocean observations and a general circulation model. *J. Geophys. Res.*, **107**, 3118.

Stewart, R.W., 1974: The air sea momentum exchange. *Boundary-Layer Meteorol.*, **6**, 151–167.

Tennekes, H., 1973 : The logarithmic wind profile. *J. Atmos. Sci.*, **30**, 234–238.

Trenberth, K.E., W.G. Large and J.G. Olson, 1989: The effective drag coefficient for evaluating wind stress over the ocean. *J. of Climate***12**, 1508–1516.

UNESCO, 1985: Discharge of selected rivers of the world, vol. I, II, III (parts I, II, III, IV), UNESCO, Paris

Wang, W. and M.J. McPhaden, 2001: What is the mean seasonal cycle of surface heat flux in the equatorial Pacific? *J. Geophys. Res.*, **106**, 837–857.

WGASF, 2000: Intercomparison and validation of ocean-atmosphere energy flux fields. Final Report of the Joint WCRP/SCOR Working Group on Air-Sea Fluxes. P.K. Taylor (Ed.), 358pp.

Wijffels, S.E., 2001: Ocean transport of freshwater. In "Ocean Circulation and Climate", Eds. G. Siedler, J. Church and J. Gould, International Geophysics Series, **77**, Academic Press, 475–488.

Xie, P. and P.A. Arkin, 1996: Analyses of global monthly precipitation using gauge observations, satellite estimates, and numerical model predictions. *J. of Climate*, **9**, 840–858.

Yelland, M.J. and P.K. Taylor, 1996: Wind stress measurements from the open ocean. *J. Phys. Oceanogr.*, **26**, 541–558.

Zhang, Y.C., W. B. Rossow, A. A. Lacis , V. Oinas and M.I. Mishchenko, 2004: Calculation of radiative flux profiles from the surface to top-of-atm osphere based on ISCCP and other global datasets: Refinements of the radiative t ransfer model and the input data. *J. Geophys. Res.*, **109**, In Press.